REPORT DOCUMENTATION PAGE

Form Approved OMB NO. 0704-0188

1. REPORT DATE (DD-MM-YYYY)	2. REPORT TYPE	3. DATES COVERED (From - To)
15-12-2014	Ph.D. Dissertation	-

4. TITLE AND SUBTITLE	5a. CONTRACT NUMBER
Water Uptake Profile In a Model Ion-Exchange Membrane: Conditions For Water-Rich Channels	W911NF-10-1-0520
	5b. GRANT NUMBER
	5c. PROGRAM ELEMENT NUMBER
	611103

6. AUTHORS	5d. PROJECT NUMBER
Daniel C. Herbst	
	5e. TASK NUMBER
	5f. WORK UNIT NUMBER

7. PERFORMING ORGANIZATION NAMES AND ADDRESSES	8. PERFORMING ORGANIZATION REPORT NUMBER
Colorado School of Mines 1500 Illinois Street, Guggenheim Hall, Room 130 Golden, CO 80401 -1887	

9. SPONSORING/MONITORING AGENCY NAME(S) AND ADDRESS (ES)	10. SPONSOR/MONITOR'S ACRONYM(S)
U.S. Army Research Office P.O. Box 12211 Research Triangle Park, NC 27709-2211	ARO
	11. SPONSOR/MONITOR'S REPORT NUMBER(S)
	58161-CH-MUR.59

12. DISTRIBUTION AVAILIBILITY STATEMENT

Approved for public release; distribution is unlimited.

13. SUPPLEMENTARY NOTES

14. ABSTRACT

Ionic conductivity in a polymeric fuel cell requires water uptake. Previous theoretical stud- ies of water uptake used idealized parameters. We report a parameter-free prediction of the water-swelling behavior of a model fuel cell membrane. The model polymers, poly(methyl- butylene)-block-poly(vinylbenzyl-trimethylamine) (PMB-b-PVBTMA), form lamellar do- mains that absorb water in humid air. We use the Scheutjens-Fleer methodology to predict the resulting change in lamellar structure and compare with x-ray scattering. The results suggest locally

15. SUBJECT TERMS

Anion Exchnage Membrane, ion transport, water transport

16. SECURITY CLASSIFICATION OF:			17. LIMITATION OF ABSTRACT	15. NUMBER OF PAGES	19a. NAME OF RESPONSIBLE PERSON
a. REPORT	b. ABSTRACT	c. THIS PAGE			Andrew Herring
UU	UU	UU	UU		19b. TELEPHONE NUMBER
					303-384-2082

Report Title

Water Uptake Profile In a Model Ion-Exchange Membrane: Conditions For Water-Rich Channels

ABSTRACT

Ionic conductivity in a polymeric fuel cell requires water uptake. Previous theoretical stud- ies of water uptake used idealized parameters. We report a parameter-free prediction of the water-swelling behavior of a model fuel cell membrane. The model polymers, poly(methyl- butylene)-block-poly(vinylbenzyl-trimethylamine) (PMB-b-PVBTMA), form lamellar do- mains that absorb water in humid air. We use the Scheutjens-Fleer methodology to predict the resulting change in lamellar structure and compare with x-ray scattering. The results suggest locally uniform water distributions. However, under conditions where a PVBTMA and water mixture phase-separate, the two phases arrange into stripes with a dilute stripe sandwiched between two concentrated stripes. A small amount of water enhances conduc- tivity most when it is partitioned into such channels, improving fuel-cell performance.

THE UNIVERSITY OF CHICAGO

WATER UPTAKE PROFILE IN A MODEL ION-EXCHANGE MEMBRANE:

CONDITIONS FOR WATER-RICH CHANNELS

A DISSERTATION SUBMITTED TO

THE FACULTY OF THE DIVISION OF THE PHYSICAL SCIENCES

IN CANDIDACY FOR THE DEGREE OF

DOCTOR OF PHILOSOPHY

DEPARTMENT OF PHYSICS

BY

DANIEL C. HERBST

CHICAGO, ILLINOIS

DECEMBER 2014

CONTENTS

LIST OF FIGURES

LIST OF TABLES

ACKNOWLEDGMENTS

Thanks to my thesis committee, Profs. Thomas A. Witten, Wendy W. Zhang, Ka Yee C. Lee, and Emil J. Martinec, for making time to meet and read the manuscript. I would especially like to thank my advisors, Tom and Wendy. They have been my role models throughout graduate school, and I have learned so much from them, about science and otherwise. I would not have made it to this point without their dedication and support.

ABSTRACT

Ionic conductivity in a polymeric fuel cell requires water uptake. Previous theoretical studies of water uptake used idealized parameters. We report a parameter-free prediction of the water-swelling behavior of a model fuel cell membrane. The model polymers, poly(methyl-butylene)-block-poly(vinylbenzyl-trimethylamine) (PMB-b-PVBTMA), form lamellar domains that absorb water in humid air. We use the Scheutjens-Fleer methodology to predict the resulting change in lamellar structure and compare with x-ray scattering. The results suggest locally uniform water distributions. However, under conditions where a PVBTMA and water mixture phase-separate, the two phases arrange into stripes with a dilute stripe sandwiched between two concentrated stripes. A small amount of water enhances conductivity most when it is partitioned into such channels, improving fuel-cell performance.

CHAPTER 1

INTRODUCTION

1.1   Alkaline-exchange membranes

Fuel cells oxidize fuel in a controlled way to efficiently convert the stored energy into electrical power. They work by performing the oxidation reaction in two steps; splitting fuel molecules at the anode and oxygen molecules at the cathode. In general, the purpose of the electrolyte is to promote transport of the reacting ions, inhibit transport of the opposite charges, and prevent cross-over of fuel or oxygen. Fuel cells can be categorized according to the composition of the electrolyte, since this determines the operating conditions. Our goal is to develop electrolytes for consumer applications, similar to lithium-ion batteries but with better energy density and rapid refueling [3]. Low-temperature electrolyte types include aqueous alkaline, proton-exchange polymer membrane, and alkaline polymer membrane. The first two are well studied and have drawbacks; while alkaline exchange membranes solve these issues, more research is needed to improve their performance.

Aqueous alkaline electrolytes such as potassium hydroxide (KOH) trace their beginnings to the earliest fuel cell designs by Christian Schönbein and Sir William Grove in 1839 [4]. This type was employed by NASA on Apollo and Space Shuttle missions, due to their best-in-class efficiency [5,6]. A big problem with KOH electrolytes, however, is their failure when exposed to carbon dioxide. For example, in KOH electrolytes, potassium carbonate crystals form, eventually clogging the system [7–9]. In systems where it would be impractical to remove carbon dioxide, aqueous electrolytes are not feasible.

Polymer membrane electrolytes can solve the problems of liquid electrolytes. Currently, most such electrolytes use Nafion™ (DuPont) [10], a proton conducting polyelectrolyte. The two half-reactions do not occur readily in the acidic environment induced by

proton-exchange membranes. Therefore, platinum is needed to catalyze the reactions; this is uneconomical. Also, platinum catalysts are poisoned by trace amounts of carbon monoxide, requiring carbon-free fuels. As an alternative, many in the community have recently turned their attention to alkaline fuel cells [11].

Alkaline-anion-exchange-membrane (AEM) fuel cells can solve the problems of both liquid alkaline fuel cells and Nafion™ fuel cells. Due to their dimensional stability, they are not poisoned by CO_2. Also, they can operate using a range of catalysts, such as nickel, since the reaction rates are much higher in an alkaline environment [8,12,13]. These features allow the use of carbon-containing fuels such as methanol, instead of pure hydrogen, and unprocessed air [3]. Currently, however, Nafion™ fuel cells outperform their alkaline-membrane counterparts in power density: Nafion™ has achieved $720\,mW/cm^2$ at $75°C$ with Nafion-112™ [11], compared to for example, $372\,mW/cm^2$ at $50°C$ with a PBI-KOH membrane [14]. Therefore, more research is needed to make alkaline membranes suitable for consumer applications.

Commonly used ionic groups for AEMs include ammonium, phosphonium, and sulphonium [15,16]. For this paper, we analyze a diblock copolymer where the hydrophilic block consists of polystyrene with a trimethyl ammonium side chain, poly(vinylbenzyl-trimethylamine)$[Br^-]$, referred to as PVBTMA. PVBTMA was first investigated as the hydrophilic block in an anion-exchange membrane by [17]. The membrane had an ionic conductivity roughly 4 times lower than Nafion™-115, but with roughly 10 times less methanol crossover. Therefore, the ratio of ion conductivity to fuel crossover was better than Nafion™-115, which makes it a promising electrolyte material.

The research reported below is part of a team sponsored by the U. S. Army through a Multidisciplinary University Research Initiative (MURI). One of the main goals of the project is to study the fundamental properties of alkaline anion-exchange membranes and validate these predictions. Accordingly, this paper explores PVBTMA (Figure 3.1) joined

2

to a hydrophobic polymer poly(methyl-butylene) to create a lamella-forming diblock. The PVBTMA was synthesized by colleagues E. Bryan Coughlin and Tsunghan Tsai at the University of Massachusetts Amherst and is described elsewhere [1].

1.2   Water distribution

Motivation   Hydroxide ion transport through the membrane is fundamentally dependent on the amount and distribution of water within the membrane. The most important transport mechanism is the Grotthuss (hopping) mechanism, where the "missing" proton in OH^- is passed along like a bucket brigade from H_2O to H_2O. This allows the negative charge to diffuse without having to move heavy oxygen atoms. This mechanism requires enough water molecules to sufficiently solvate the ion. (An analogous mechanism occurs in acidic fuel cells to pass along the "extra" proton in H_3O^+.) A slower mechanism is where the OH^- itself diffuses through water (vehicular transport). This is related to the third mechanism, where the ion is passed from one N^+ to another along the polymer itself. Finally, there is water convection, which is a second order effect—ions drag water that in turn drag other ions. Due to reasons not completely understood, ionic diffusion is roughly twice as fast for H_3O^+ compared to OH^- : $9.3\times$ vs. $5.3 \times 10^{-9}\,m^2s^{-1}$ in $25°$ C water [18]). Therefore, it is a challenge to make OH^- fuel cells conduct as well as H^+ fuel cells.

For practical reasons, fuel cells are operated with relatively dry membranes. If ion conductivity were the only consideration they would be much wetter [19]. One problem with too much water is that water can flood the gas diffusion layers, the regions designed to allow the input gasses to contact the catalyst [20]. Another problem is that the membrane can become weak and develop holes, especially after repeated wet-dry cycles [21]. Under these constraints, the way to maximize conductivity is to make the membrane heterogeneous on a microscopic scale, containing regions for structure and regions for ion diffusion. The

3

ion-bearing regions absorb water, creating pathways for ion conduction. Examples include interpenetrating polymer networks [22] and diblock copolymers [23], where each chain of hydrophilic polymer is connected to a hydrophobic polymer.

Morphology   The model PMB-b-PVBTMA diblock studied here forms alternating layers of PMB and PVBTMA. Each connection point is constrained to lie at the interface between a PMB block and its adjoining PVBTMA block. PMB, a rubbery material also known as hydrogenated polyisoprene, was chosen as a compromise between structural rigidity and flexibility, allowing the membrane to maintain a lamellar structure while still being able to swell with water.

Di-block copolymers can produce a plethora of periodic structures. Depending on the volume ratio of the hydrophilic and hydrophobic parts, and their degree of incompatibility, a solution of the diblock copolymers will micro-phase separate into a particular morphology [24]: lamellae, micelles [25], cylinders, spheres, gyroids, etc. In Nafion™ for example, the conducting parts of the polymer (sulfonic acid side chains) are believed to form networks of connected micelles within the hydrophobic bulk [26]. The phase space of morphologies as a function of molecular weight and degree of repulsion has been determined from field theory [27]. The different morphological regimes of a similar diblock co-polymer, PMB-block-poly-(styrene-sulfonate), are classified in experiment [28] and coarse-grain simulations [29]. For simplicity, we focus on a lamellar morphology. The interface transition width and interface surface tension has been analyzed with field theory calculations, and again depends on molecular weight and degree of repulsion [30,31]. In our calculations, we ignore any effects of the PMB-PVBTMA interaction except to set the areal (grafting) density of the PVBTMA chains, as described in Section 3.3. We assume that PMB and PVBTMA are dissimilar enough that the interface between the two is flat up

4

to the resolution of the calculation. The orientation of the morphology can be aligned using electric potentials or mechanical stress, minimizing the effect of tortuosity [32].

Water channels   The results of this study suggest a new way to engineer morphologies beneficial to durability and ion transport. The type of morphology discussed in the previous paragraph does not depend on water absorption; membranes are usually cast dry, and the morphology depends on the hydrophilic-to-hydrophobic polymer in this state. This dependence leads to using more hydrophilic polymer than would otherwise be ideal in order to establish a desirable morphology. We propose that an ideal membrane should have a low hydrophilic-to-hydrophobic ratio, for several reasons. First, this is the case for Nafion, the gold standard for PEM membranes; its unique pore structure makes it possible. Second, ion diffusivity in polyelectrolyte solutions increases exponentially or even faster with increasing water content, plateauing beyond roughly a 50% water mixture [1]. For a given amount of water, it is much better to have it concentrated into conducting channels. Besides in Nafion, most fuel cell membranes do not reach such high water fractions, even within their conducting regions. This low water content is an intentional trade-off. Too much water causes the hydrophilic blocks to swell significantly and become gel-like, but this is only a problem if the hydrophilic polymers constitute a major portion of the membrane. In short, we would like to be able to use a small amount of hydrophilic polymer and yet still specify the morphology. Here is where water channels are important. Our model copolymer, for example, is composed of roughly equal parts PMB and PVBTMA, producing a well-connected lamellar morphology. If we could design the membrane to absorb water preferentially into narrow stripes down the center of each lamella, the rest of the PVBTMA block would remain dry and stable. From our preliminary results, we discovered that this can indeed occur if PVBTMA has a solubility gap, at the conditions that generate a two-phase coexistence [33,34]. As an added benefit, we proposed that dissociated ions from the

5

dense phase can leach into the dilute phase, enhancing conductivity even more. This turns out to be a negligible effect in this case (see Section 7.4), but could be exploited in future designs. After we proposed these ideas, there has been experimental evidence for lamellar water channels in a polystyrene-block-poly(styrene-sulfonate) membrane [35]. One of the goals of this paper is to use numerical modeling to determine the properties of these water channels and under what conditions they form in a real system.

Theory background Three classes of theory/simulation are used to study polymers: molecular dynamics, coarse-grained dynamics, and field theory [36]. The first, molecular dynamics simulations, evolve the position and velocity of each atom in the system according to various force models and random thermal noise. Currently, these are too computationally intensive to be able to model and equilibrate an entire lamella. Even if they could, molecular dynamics would be overkill for studying an entire lamella; they are better suited to studying small-scale effects such as ion hopping. For example, our MURI collaboration has studied ion transport in small systems of PVBTMA [37]. The second class, coarse-grained dynamics, is similar but replaces groups of atoms with pseudo-particles. These models can be scaled up to the size of a lamella. A big contribution of this method was to confirm the validity of the field theory methods [38], one of which is used in this study. Field theory methods are concerned with larger-scale effects and near-equilibrium behavior, usually ignoring dynamics and stochastics. They are rooted in the similarity between a polymer's partition function and that for a diffusing particle [39,40]. Some ideal cases with symmetry can be studied analytically [40,41]. Numerically, they can be studied using spectral methods that track Fourier modes [27], or using real space methods. One of these, the Scheutjens-Fleer method [42,43], is based on weighted random walks on a lattice, with the lattice spacing set by the polymer's flexibility according to the freely-jointed-chain model. The Scheutjens-Fleer method is equivalent to the discretized diffusion

equation with numerical derivatives. Therefore, so-called continuum methods [30,44] are equivalent, but may over-smooth features if the lattice spacing is too fine. Different lattice geometries produce equivalent results as long as the proper correction is made to the lattice spacing [45]. These theories have been applied to two systems relevant to this work: polymer brushes and diblock copolymer lamellae.

Polymer brush background   Similar to an end-grafted *polymer brush*, the PVBTMA polymers in our system each have one end constrained to lie at the hydrophilic-hydrophobic interface, with the other end free. Polymer brushes are well studied. The first experiments measured the force between two facing polymer brushes immersed in a good solvent [46] and poor solvent [47]. Early theoretical work found the mean-field scaling behavior of the brush *height*, or distance from the interface [40]. In the limit of high molecular weight, the polymer profile was found to be parabolic [41]. The scaling arguments were re-derived for charged polymer brushes in a strong salt solution and found to behave equivalently to neutral brushes in a good solvent [48]. Numerical studies of two overlapping polymer brushes [44,49] have mostly focused on ideal Flory-Huggins solvents with an interaction parameter, χ, near 0.5 – i.e., the *theta point*, where the solvent is just poor enough to exactly cancel the polymer's swelling due to self avoidance, and the polymer's self-interaction vanishes. The transition from poor to good solvent has been studied by molecular dynamics simulations [38,50] and confirmed through neutron scattering [51].

This work in context   The aim of this paper is to use established polymer brush theory to study ionic copolymer membranes, with no free parameters. Experimental progress includes X-ray scattering on membranes with a selective solvent [52]. Theoretical progress includes a mean-field calculation of polymer brush profiles [44], but most investigations assumed a Flory-Huggins equation of state near the theta point. This work is the first work

that we are aware of that solves for the solvent distribution within a membrane with no free parameters. Specifically, we model the hydrophilic lamella as two facing polymer brushes and calculate how the lamella swells as a function of ambient humidity (water activity). We calculate the water profile within a lamella, since it is known from polymer brushes that water varies spatially due to competition between wetting and chain stretching. To calculate the spatial dependence, we solve the self-consistent field equations using the Scheutjens-Fleer method [42,43], a standard method for studying polymer brushes outlined in Section 2.3. The calculation requires three main inputs. First, the flexibility of the hydrophilic chains is inferred from literature values of similar polymers (Section 3.2). Second, the solubility of the hydrophilic block is measured for a sample of isolated hydrophilic block, not tethered to a hydrophobic block (Section 3.4). Third, the grafting density of hydrophilic block at the interface, which depends on humidity, is inferred from small-angle X-ray scattering (Section 3.3). Thus, all the parameters used for the calculation are experimentally determined. Finally, we attempt to verify the predictions as much as possible from independent experimental measurements.

Overview of this report   Chapter 4 shows the result of the calculations. Under under most conditions (absent a phase separation), water is predicted to nearly uniformly absorb into the hydrophilic regions of PVBTMA. In that case, the overall membrane conductivity is straightforward to estimate. The amount of water absorbed determines the polymer concentration in the hydrophilic blocks. If one knows the conductivity as a function of concentration, then the overall conductivity can be extrapolated. If, however, there are distinct regions with more and less water, this simple calculation is no longer possible. As a concrete example, our calculations predict that under some conditions, water-rich slabs ("stripes") may form at the center-plane of some hydrophilic lamellae. Heterogeneous water absorption is expected to conduct ions better than homogeneous absorption of the same

amount of water, since conductivity increases faster-than-linearly with water content in this regime [19]. Therefore, understanding the conditions that encourage uneven water absorption is important for developing fuel cells that conduct ions well without absorbing so much water that they lose integrity.

CHAPTER 2

CALCULATION METHODOLOGY

2.1 Random walk representation

The Scheutjens-Fleer model [42,43] is intended to describe the structure on the length scale of several chain persistence lengths, that is, it is a mean-field model. The mutual interaction of the monomers, including mutual avoidance, gives rise to a free energy cost for inserting a monomer at any position. This cost approaches a statistical average when the density of monomers is high. For closely packed chains, this is a good assumption, since each thermodynamically significant segment of polymer interacts with several others at any given time [53]. All of our predictions are in the polymer-dense regime where the mean-field formulation applies. We study a lamellar geometry uniform in the *x* and *y* coordinates with variation only in *z* (perpendicular to the hydrophilic/hydrophobic interface, see Fig. 2.1).

At the scales considered, the specifics of the local chain configurations and their interactions become unimportant and each polymer can be represented as a random walk on a cubic lattice. The separation between lattice sites is chosen so that the random walks capture the real flexibility of the polymer at the theta point. That is, the lattice parameter is set to be the *Kuhn length*, ℓ_K, of the polymer (twice the persistence length). The Kuhn length is a measure of how coiled the polymer is at the theta point–the point at which the solvent is just poor enough to exactly cancel the polymer's swelling due to self avoidance. That is, a free polymer in dilute solution at the theta point behaves as a non-self-avoiding random walk with step lengths equal to the Kuhn length. To define it exactly, we require [54]:

1. the mean squared end-to-end distance matches the polymer at theta conditions: $n\ell_K^2 = \langle r^2 \rangle_0$, where n is the number of segments, or Kuhn steps composing the random walk, and $\langle r^2 \rangle_0$ is the average end-to-end span of the polymer at theta conditions.

2. the total length of the random walk is equal to the length of an ideal chain that is fully extended while still maintaining the covalent bond angle, $\theta_b = 109.5°$, of the hydrocarbon backbone: $n\ell_K = n_b \ell_b \sin \theta_b / 2$, where n_b is the number of backbone bonds, ℓ_b is the bond length (154 pm).

Combining the requirements gives:

$$\ell_K = \frac{\langle r^2 \rangle_0}{n_b \ell_b \sin \theta_b / 2} = \frac{C_\infty \ell_b}{\sin \theta_b / 2}, \qquad (2.1)$$

$$n = \frac{n_b \sin^2 (\theta_b / 2)}{C_\infty}, \qquad (2.2)$$

where $C_\infty \equiv \langle r^2 \rangle_0 / n_b \ell_b^2$ (in the limit $n_b \to \infty$) is the experimentally measured *characteristic ratio*, as discussed in Section 3.2.

The calculation space, $\vec{r}$, is discretized into a square Kuhn-length lattice. In particular, we introduce an integer variable ζ, which counts the number of Kuhn steps from the interface: $z = \zeta \ell_K$. Points within 1 Kuhn length of the interface are grouped together as $\zeta = 1$, points within 1 to 2 Kuhn lengths of the interface are $\zeta = 2$, etc. Let there be m lattice lengths between the interface and the lamella's mid-plane so that z ranges from 1 to m. This fixes the swelled hydrophilic lamellar width to $2m\ell_K$ (Section 7.3 shows how to accommodate half-integer widths). The width depends on the amount of solvent admitted into the brush, as determined by the experimental conditions outlined below. Other functions such as ϕ are similarly discretized. We may refer to $\phi(z)$ and $\phi(\zeta)$ interchangeably depending on context.

2.2 Self consistency

The following is a brief overview for the method of finding $\phi_{\text{avg}}(\zeta)$, the mean-field polymer volume-fraction profile as a function of position. We start with an ansatz that the profile is given by some assumed $\phi_{\text{avg}}(\zeta)$. A given Kuhn segment inserted at height ζ interacts with $\phi_{\text{avg}}(\zeta)$ via the chemical potential, $\mu_K(\zeta)$. This potential depends only on the local average volume fraction, so $\mu_K(\zeta)$ or $\mu_K(\phi(\zeta))$ may be used interchangeably. The functional form of $\mu_K(\phi)$ can be obtained independently through experimental measurement, as discussed in Section 3.4, and we thus presume it to be known. This is used here in a restricted sense to mean the energy required to insert a Kuhn segment into a uniform solution whose volume fraction is $\phi_{\text{avg}}(\zeta)$; therefore, unlike the full chemical potential, $\mu_K(\zeta)$ varies in space (from entropic effects due to the tethering of one end to the interface).

To test whether the ansatz $\phi_{\text{avg}}(\zeta)$ is self-consistent, now consider a single test chain among the many. Every spatial configuration of the polymer (for examples see Fig. 2.1) exists with a certain probability, determined by $\mu_K(\zeta)$ (to be spelled out in Section 2.3). By averaging all the possible configurations we can calculate the test polymer's average volume-fraction profile, $\langle \phi(\zeta) \rangle$. If the solution is self-consistent, then the mean-field distribution equals the test-chain distribution:

$$\phi_{\text{avg}}(\zeta) = \langle \phi(\zeta) \rangle. \tag{2.3}$$

In general, the first guess will not be self-consistent, but we can use an iterative process to converge to the self-consistent solution. Equation 2.3 is a set of m single-variable equations, one for each ζ. We solve this using the Newton-Raphson method [55], producing a self-consistent $\phi_{\text{avg}}(\zeta)$. That is, we look for the root (or roots) of the equation $f(\zeta) = \phi_{\text{avg}}(\zeta) - \langle \phi(\zeta) \rangle$ using the Jacobian $J_{ij} = \partial f(\zeta_i)/\partial \phi_{\text{avg}}(\zeta_j)$. Note that

$\langle \phi (\zeta) \rangle$ is a function of $\phi_{\mathrm{avg}}(\zeta)$ as is spelled out in the next section. Therefore, $J_{ij} = \delta_{ij} - \partial \langle \phi (\zeta_i) \rangle / \partial \phi_{\mathrm{avg}} (\zeta_j)$, where δ_{ij} is the Kronecker delta function. An iteration is $\phi_{\mathrm{avg}}(\zeta_i) \rightarrow \phi_{\mathrm{avg}}(\zeta_i) - \lambda J_{ij}^{-1} f(\zeta_j)$, where $\lambda \in (0, 1]$ as described in Numerical Recipes [55]. We implemented the scheme in Mathematica. Each Newton step takes approximately 1 second to compute on a single, modest processor. It takes roughly 10–100 steps to converge to within 8 decimal places, with only occasional intervention required to nudge the algorithm away from a local minimum.

2.3 Scheutjens-Fleer method

The following procedure calculates $\langle \phi (\zeta) \rangle$ for the single test chain by efficiently summing up the Boltzmann weights for all the random walk configurations on the lattice. This is permissible since the lattice has Kuhn-length spacing: when considering the set of random walks the polymer can follow on such a lattice, its bending energy and self-interaction energy are implicitly included. Therefore, the only interaction that goes into the Boltzmann factors is $\mu_K (\zeta)$, the interaction between polymer segment and the water-polymer solution at ζ. By construction, $\mu_K (\zeta)$ includes the total free energy to insert a segment at ζ, including making space for it under osmotic pressure, or equivalently, displacing an equivalent volume of water. Therefore, the Boltzmann factor for each segment is just $\exp[-\mu_K (\zeta) / k_B T]$. For a segment at position $\vec{r}$, the ζ coordinate is its non-dimensionalized projection onto the z-axis: $\zeta = \vec{r} \cdot \hat{z} \ell_K^{-1}$. Given a 3-d Kuhn lattice random walk, $\{\vec{r}\}$, its relative probability of occurrence, R, at fixed volume is simply the product of all the segment Boltzmann factors:

$$R(\{\vec{r}\}) \;=\; \prod_{j=1}^{n} \exp\left[-\mu_K\left(\vec{r}_j \cdot \hat{z} \ell_K^{-1}\right) / k_B T\right]. \tag{2.4}$$

13
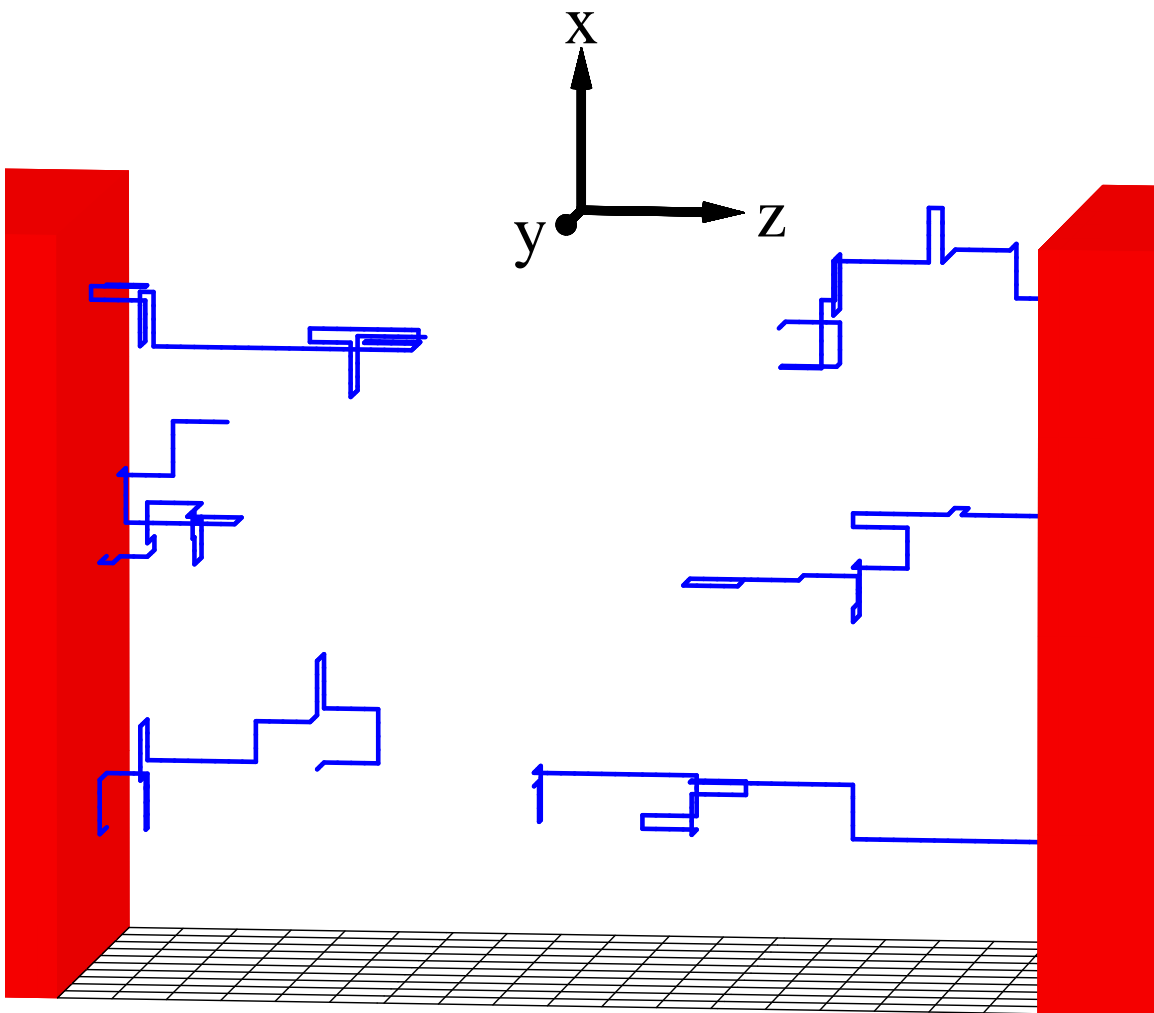
Figure 2.1. Illustration of the calculation procedure. Six statistically representative PVBTMA Kuhn-lattice walks are shown (blue), flanked by PMB interfaces (red). Based on a guess for the average profile $\phi_{\mathrm{avg}}(z)$, and the interaction potential $\mu_K(\phi)$, the Scheutjens-Fleer calculation computes the Boltzmann-weighted average profile, $\langle \phi(\zeta) \rangle$. When $\langle \phi(\zeta) \rangle = \phi_{\mathrm{avg}}(\zeta)$, the solution is self-consistent.

Since the lattice is Cartesian, there are of order $(2 \cdot 3)^n$ unique chain conformations. This can be reduced. Instead of finding the relative probability of a given $\{\vec{r}\}$, we can find the relative probability of a projection onto ζ-coordinates, $\{\zeta\}$. $\{\zeta\}$ is similar to a 1-d random walk, but each coordinate can be $+1$, 0, or -1, relative to the preceding coordinate. A $+\ell_K \hat{z}$ step maps to $+1$, $-\ell_K \hat{z}$ to -1, and $\pm \ell_K \hat{x}$ and $\pm \ell_K \hat{y}$ all map to 0. This leads to a redundancy factor, λ :

$$\lambda \left(\zeta_j - \zeta_{j-1} \right) = \begin{cases} 1 & \left(\zeta_j - \zeta_{j-1} \right) = \pm 1 \\ 4 & \left(\zeta_j - \zeta_{j-1} \right) = 0 \end{cases}. \tag{2.5}$$

The first Kuhn segment for all the chains occupies $\zeta = 1$ and so does not have an associated λ. The resulting expression for relative probability is:

$$\frac{R(\{\zeta\})}{\exp\left[\frac{-\mu_K(1)}{k_B T}\right]} = \prod_{j=2}^{n} \lambda \left(\zeta_j - \zeta_{j-1} \right) \exp\left[\frac{-\mu_K\left(\zeta_j\right)}{k_B T} \right]. \tag{2.6}$$

The inputs, $\{\zeta\}$, still have many combinations. The direct calculation for the resulting test-chain profile is given by summing over all chain conformations and binning their segment positions:

$$\left\langle \phi \left(\tilde{\zeta} \right) \right\rangle \propto \sum_{\{\zeta\}} R(\{\zeta\}) \sum_i \delta_{\zeta_i, \tilde{\zeta}}, \tag{2.7}$$

where δ is the Kronecker delta function. Scheutjens and Fleer discovered a computational trick to calculate $\langle \phi \rangle$ in only order $m \cdot n$ computations. It makes use of two Green's functions. First, $G_{1 \to i}^{1 \to \zeta}$, defined as the sum of partial Boltzmann products for segment 1 through segment i (i.e., $R(\{\zeta\})$ in 2.6 with $n = i$) for all possible chain conformations beginning at the interface ($\zeta = 1$) and ending with segment i in layer ζ. Similarly, $G_{i \to n}^{\zeta \to *}$ is defined as the sum of partial Boltzmann products for segment i through final segment n for all

15

conformations with segment i in Kuhn cell ζ (the $'*'$ indicates that the final position is unspecified). Then by construction, the probability of finding segment i in cell ζ is:

$$P_i(\zeta) \equiv \alpha G_{1\to i}^{0\to\zeta} G_{i\to n}^{\zeta\to*} / \exp\left[-\mu_K(\zeta)/k_B T\right], \qquad (2.8)$$

where α is a normalization factor. The divisor is to account for the fact that the ith Boltzmann factor is counted in both Green's functions. The normalization factor, α, can be determined by requiring $P_1(1) = 1$; that is, all the 1st segments originate at the interface and exist in the 1st Kuhn cell. The efficiency trick comes from the fact that the Green's functions can be generated inductively. The process is illustrated in section 7.2. Starting with the distribution of segment 1, assumed to all be attached at the interface,

$$G_{1\to1}^{1\to\zeta} = \begin{cases} \exp\left[-\mu_K(1)/k_B T\right] & \zeta = 1 \\ 0 & \zeta > 1 \end{cases}.$$

We may build expressions for G involving further steps along the chain inductively:

$$G_{1\to i+1}^{1\to\zeta} = \exp\left[-\mu_K(\zeta)/k_B T\right] \times$$

$$\times \begin{cases} 0 & \zeta < 1 \\ G_{1\to i}^{1\to\zeta-1} + 4G_{1\to i}^{1\to\zeta} + G_{1\to i}^{1\to\zeta+1} & 1 \le \zeta < m \\ G_{1\to i}^{1\to\zeta-1} + 5G_{1\to i}^{1\to\zeta} & \zeta = m \end{cases} \qquad (2.9)$$

The overall prefactor is the Boltzmann factor associated with the $(i+1)$th Kuhn segment. The first case gives the effect of the (assumed) impenetrable diblock interface at $z = 0$. The second case applies to the bulk of the lamella, away from the boundaries. The terms arise from the different ways in which the random walk can arrive at ζ after i steps.

16

Relative to the $(i+1)th$ segment, the ith segment can either be $+\hat{z}$ (first term), $\pm\hat{x}$ or $\pm\hat{y}$ (second term), or $-\hat{z}$ (third term). The third case creates a mirror boundary condition at $z = m\ell_K$: if the $(i+1)$th segment would cross the mirror, it is instead reflected back [49]. The mirror is on the face of the $\zeta = m$ cell, so if the $(i+1)$th segment is in the $+z$ direction, it starts and ends at $\zeta = m$. This, plus the $\pm x$ and $\pm y$ steps gives the factor of 5. A variation of this boundary condition is shown in Section 7.3. This representation is equivalent to evaluating two sets of polymer brushes, one on the left interface and one on the right, overlapping in the middle. To get the polymer distribution in the full lamella, the left profile is simply reflected about $z = m\ell_K$.

A second set of Green's functions needs to be calculated starting from the free end of the chain and working back toward the tethered end: $G_{n\rightarrow n}^{\zeta\rightarrow *} = \exp\left[\mu_i\left(\zeta\right)/k_BT\right]$, and i is iterated downward:

$$G_{(i-1)\rightarrow n}^{\zeta\rightarrow *} = \exp\left[-\mu_K\left(\zeta\right)/k_BT\right]\times$$

$$\times \begin{cases} 0 & \zeta < 1 \\ G_{i\rightarrow n}^{\zeta-1\rightarrow *} + 4G_{i\rightarrow n}^{\zeta\rightarrow *} + G_{i\rightarrow n}^{\zeta+1\rightarrow *} & 1 \leq \zeta < m \\ G_{i\rightarrow n}^{\zeta-1\rightarrow *} + 5G_{i\rightarrow n}^{\zeta\rightarrow *} & \zeta = m \end{cases} \qquad (2.10)$$

For each position ζ, the polymer density due to the Boltzmann-weighted configurations can be calculated by adding up the contributions due to every ith segment from $i = 1$ to n, and normalizing:

$$\langle\phi\left(\zeta\right)\rangle = \left(\frac{\sigma V_K}{\ell_K}\right)\sum_{i=1}^{n}P_i\left(\zeta\right). \qquad (2.11)$$

The prefactor in parentheses is the fraction of volume that the initial segments collectively occupy within the first lattice cell, and depends on the average volume of a Kuhn segment, V_K; the Kuhn length, ℓ_K; and, the grafting density, σ, defined as the number of PVBTMA

17

attachments divided by the interfacial surface area. This equation is used to compute the iterative refinements outlined in Section 2.2 that result in a self-consistent $\phi_{\text{avg}}(\zeta)$.

In summary, this method calculates the polymer distribution for a specific lamellar width $2m\ell_K$. In experiments, however, the control variable for swelling is the water activity, a (the ambient relative humidity with which the membrane is in equilibrium). To relate the two, we note that along the center plane of the calculation, $z = m\ell_K$, the potential is symmetric and so the polymers behaves locally as a random walk. Hence, they cannot support an osmotic pressure, and so the chemical potential of water at the center plane is the same as that of a water molecule in an untethered polymer solution of concentration ϕ. This is the same $\mu_w(\phi)$ determined in Section 3.4.2, below. That is, the water activity of the calculation output, $\phi_{\text{avg}}(\zeta)$, is given by:

$$a = \exp \frac{\mu_w\left(\phi_{\text{avg}}(m)\right)}{k_B T}. \tag{2.12}$$

2.4   Calculation of μ_K

The previous section requires the work, $\mu_K(\zeta)$, to take an isolated Kuhn segment and insert it into layer ζ at fixed volume. Evidently, this only depends on the local polymer volume fraction, ϕ, so we seek the function $\mu_K(\phi)$, and $\mu_K(\zeta) = \mu_K(\phi(\zeta))$. The quantity μ_K must be inferred from experiment (Section 3.4), which measures the chemical potential of water, $\mu_w(\phi, p_0)$, as a function of concentration, ϕ, at ambient pressure p_0. Consider a large volume, V, of solution at volume fraction ϕ, pressure p, and temperature T. For convenience, we divide the volume into N units with volume equal to the average volume, V_{H_2O}, of a water molecule. Of these, $N_w = (1 - \phi)N$ consist of water and $N_s = \phi N$ consist of polymer (we use the subscript s since the argument is applicable to any solute, not just

polymers). In terms of the Helmholtz free energy, A, μ_w is defined by:

$$\mu_w = \left(\frac{\partial A}{\partial N_w} \right)_{N_s, V, T}. \tag{2.13}$$

The derivative is performed holding fixed N_s, volume V, and temperature T. We need to find μ_s, the free energy cost to add a unit of polymer. Since the process of adding a Kuhn segment is isotropic, the Gibbs-Duhem equation [56] simplifies to: $N_s d\mu_s = -N_w d\mu_w + V dp$. In the limit where the layer is much larger than a single unit, $dp \to 0$. Therefore,

$$N_s d\mu_s = -N_w d\mu_w.$$

This equation can be integrated to give $\mu_s(\phi, p_0)$, using $(1-\phi)N_s = \phi N_w$. Holding pressure constant at p_0 and using a dummy integration variable, $\tilde{\mu}_w$:

$$\mu_s(\phi, p_0) = -\int_{-\infty}^{\mu_w} \frac{N_w}{N_s} d\tilde{\mu}_w.$$

Transforming the integration variable to ϕ, and using the dummy variable $\tilde{\phi}$,

$$\mu_s(\phi, p_0) = -\int_1^{\phi} \frac{1-\tilde{\phi}}{\tilde{\phi}} \frac{\partial \mu_w(\tilde{\phi}, p_0)}{\partial \tilde{\phi}} d\tilde{\phi}$$

Integrating by parts,

$$\mu_s(\phi, p_0) = - \frac{1-\phi}{\phi} \mu_w(\phi, p_0) - \int_1^{\phi} \frac{\mu_w(\tilde{\phi}, p_0)}{\tilde{\phi}^2} d\tilde{\phi}. \tag{2.14}$$

19

The pressure dependence can be found from one of the Maxwell relations [56],

$$\left(\frac{\partial \mu_i}{\partial p}\right)_{T,N_i,N_j} = \left(\frac{\partial V}{\partial N_i}\right)_{T,p,N_{j\neq i}}$$

The right side of this equation is just V_{H_2O}, since the unit volume for each species is taken to be the same. Therefore, both pressure derivatives are equal:

$$\left(\frac{\partial \mu_s}{\partial p}\right)_{T,N_i,N_j} = \left(\frac{\partial \mu_w}{\partial p}\right)_{T,N_i,N_j}.$$

Integrating with respect to p gives:

$$\mu_s(\phi,p) - \mu_s(\phi,p_0) = \mu_w(\phi,p) - \mu_w(\phi,p_0).$$

Using equation 2.14 and noting that at equilibrium, $\mu_w(\phi,p)$ is constant between layers, gives:

$$
\begin{aligned}
\mu_s(\phi,p) &= \text{const} - \frac{\mu_w(\phi,p_0)}{\phi} - \int_1^\phi \frac{\mu_w(\tilde{\phi},p_0)}{\tilde{\phi}^2}\,d\tilde{\phi} \\
&\equiv \mu_s(\phi).
\end{aligned}
\tag{2.15}
$$

The constant does not affect the Scheutjens-Fleer calculation and can be ignored. Finally, μ_K is simply the free energy required to insert $V_K/V_{H_2O} \approx 63$ units of polymer. Therefore,

$$\mu_K(\phi) = \left(\frac{V_K}{V_{H_2O}}\right)\mu_s(\phi). \tag{2.16}$$

Thus, μ_K does in fact only depend on the local polymer concentration, ϕ.

The self-consistency of Scheutjens and Fleer imply local equilibrium between polymer stress and osmotic pressure. However, such states need not be unique. Even in simple liquids one encounters metastable states. Similar situations can occur in the current polymer system as well.

2.5 Multiple solutions

Occasionally, there will be multiple solutions that satisfy the self-consistency equations under the same conditions. Of these solutions, the one with the lowest free energy constitutes the physically stable state. To calculate the free energy, note that the term $G_{1 \to n}^{1 \to *}$, defined by iterating equation 2.10 down to $i = 1$, is actually the complete partition function for the test chain over all 3-dimensional random walks, RW^3 :

$$Z = \sum_{\{\vec{r}\} \in RW^3} \exp\left[-W\left(\{\vec{r}\}\right)/k_B T\right],$$

where $W\left(\{\vec{r}\}\right) = \sum_{i=1}^{n} \exp\left[-\mu_K \left(\vec{r}_j \cdot \hat{z} \ell_K^{-1}\right)/k_B T\right]$ is the relative work to assemble the conformation $\{\vec{r}\}$. This relationship stems from the equivalency of equations 2.4 and 2.6. Therefore, the free energy, A, per chain is:

$$A\left[\phi\left(\zeta\right)\right] = -k_B T \log G_{1 \to n}^{1 \to *}. \tag{2.17}$$

A includes the free energy of the water per chain, since μ_K is the complete free energy to assemble the configuration given the response of the background distribution and associated osmotic pressure. A can be used to compare two systems with equal volume and equal water content per chain (equal σ). The one with the smaller A is thermodynamically favored. It turns out that A can also be used to compare between two profiles with different

amounts of water, since the hypothetical water reservoir (not the humid air) is at zero chemical potential: $\mu_w(\phi = 0) = 0$. This can be seen more clearly by introducing a hypothetical intermediary state, one in which two artificial partitions are introduced that segregate a layer of pure water in the middle of the lamella. The energy to introduce the partition is implicitly counted in A for the partitioned system, since the available system states are constrained. Then, if water is added to the center swelling the lamella, this change happens with no change in free energy, since the added water does not affect the chains outside of the partitions. When the partitions are released, the chains assume their self-consistent form, and a new A can be calculated and directly compared with the previous A.

Our calculation also assumes a variable chain areal density on the interface, σ, which the system sets by minimizing the free energy associated with the interface surface (Section 3.3). Unfortunately, σ is inferred directly from experiment so the underlying free energy contributions are unknown. Despite this missing term, which is presumed to be small for our system, we proceed to use A to distinguish between multiple solutions at the same width and/or water activity.

Care should be taken regarding discretization of the spatial coordinates. In some cases, the Scheutjens-Fleer method produces a fake solution that is artificially self-consistent in a discretized framework, but would not be self-consistent in a continuous framework. This effect occurs, for example, if there is a sudden jump in ϕ, such as at the interface of a water channel (Chapter 4). At such an interface, there is a strong energy barrier between the two phases; a point in the dilute phase cannot easily move to the concentrated phase, and vice versa. In effect, the discretization adds an implicit, unphysical force to the system that corrupts A. To find the correct water channel width, we used an annealing process. We modulated the interaction strength via V_K/V_{H_2O} until the profile was smooth, and then gradually escalated back to the correct V_K/V_{H_2O}. This process ensured a correct water channel width.

CHAPTER 3

MEASUREMENT OF PARAMETERS

In order to calculate the polymer distribution within a hydrophilic layer of the PMB-PVBTMA membrane sample, several parameters describing these polymers are needed. Section 3.1 highlights pertinent synthesis and characterization details for the PMB-b-PVBTMA membrane sample. Section 3.2 estimates the Kuhn length for PVBTMA, a measure of its flexibility. Section 3.3 describes x-ray and water uptake experiments used to determine the polymers' "grafting density" at the block interface. Finally, Section 3.4 details water uptake experiments on isolated, untethered PVBTMA, resulting in an equation of state.

3.1 Synthesis characterization

For each block of the membrane, we need the degree of polymerization and the average volume of a monomer.

Gel permeation chromatography and nuclear magnetic resonance spectrometry experiments determined that each hydrophilic block comprises on average 160 repeat units, 84% of which are PVBTMA$[Br^-]$, with the remaining 16% poly-(4-methylstyrene). Each hydrophobic block comprises on average 358 repeat units of PMB, with an isomer ratio, (1,4):(1,2):(3,4), measured to be 0.895:0.042:0.064 by mass. The polymers are relatively uniform with a polydispersity of 1.11. [1]

The density of PVBTMA$[Cl^-]$ is $1.325\,\mathrm{g/cm^3}$ [57], from which we estimate the density of PVBTMA$[Br^-]$ to be $1.60\,\mathrm{g/cm^3}$, taking account of the larger mass and larger displaced volume of Br^- compared to Cl^-. The un-brominated monomers are poly-(4-methylstyrene), which has a density of $1.106\,\mathrm{g/cm^3}$. Taking into account the 84:16 mole

23

(a) C_∞=9.85 **(b)** C_∞>9.85 **(c)** C_∞<13.4 **(d)** C_∞≈9.85
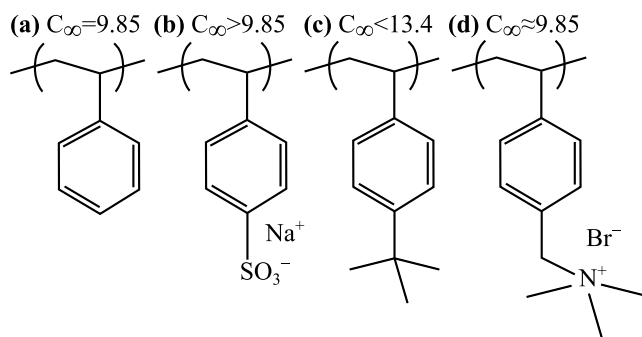
Figure 3.1. Chemical structure of polymers similar to PVBTMA with known characteristic ratios, C_∞. (a) Polystyrene, 9.85 (b) Sodium poly(styrene-sulfonate): the charged group increases C_∞ slightly due to screened charge repulsion. (c) Poly(4-tert-butylstyrene), 11.9–13.4: the trimethyl group increases C_∞ due to steric repulsion. (d) PVBTMA: its C_∞ should be within the range 9.85–13.4. We used $C_\infty = 9.85$ in the calculation.

ratio and assuming ideal mixing[1], this results in an estimated average monomer volume of $0.254\,\text{nm}^3$, and block molecular weight of 37400 amu.

For PMB, a similar isomer blend found in the literature has a density of $0.853\,\text{g/cm}^3$ [58]. This results in an average monomer volume of $0.136\,\text{nm}^3$ and block molecular weight of 25060 amu. For reference, this blend of PMB has a glass transition temperature of $-63°\text{C}$, so it is indeed rubbery and able to allow the membrane to swell.

3.2 Kuhn length

The Kuhn length, ℓ_K, has not been determined for our PVBTMA polymer, but the value can be bounded using reported measurements of the characteristic ratio, C_∞, for related polymers. PVBTMA[Br^-] (Figure 3.1 d) can be thought of as polystyrene (Figure 3.1 a) with an added trimethyl group and an electrolyte. Polystyrene has a characteristic ratio of 9.85 [59]. The trimethyl group adds a steric effect, increasing the characteristic ratio. For example, poly(4-tert-butylstyrene) (Figure 3.1c) is sterically similar and has a charac-

---

1. There may be a departure from ideal mixing, especially as $\phi \to 1$, that we do not account for.

teristic ratio in the range of roughly 11.9 to 13.4 [59]. Adding electrolytes to a polymer also tends to increase the characteristic ratio in a salt-free solution, but this effect is vanishingly small for high polymer concentration [60]. The increase in characteristic ratio, ΔC_∞, due to adding an electrolyte to each monomer can be estimated using the following Odijk expansion [61] for the relative increase in Kuhn length, $\Delta \ell_K$. For example, consider polystyrene at 50% concentration in water at $60^\circ C$. With $C_\infty^{(PS)} = 9.85$, this implies a Kuhn length of $\ell_K^{(PS)} = 1.86\,$nm (equation 2.1), a segment comprising 7.38 monomers and occupying volume $V_K^{(PS)} = 1.27\,$nm^3. The number charge density in this scenario is $n_q = 0.50 \cdot \left(1.27\,\text{nm}^3\right)^{-1}$. Then, the relative increase in the characteristic ratio is:

$$\frac{\Delta C_\infty}{C_\infty} = \frac{\Delta \ell_K^{(PS)}}{\ell_K^{(PS)}} = \frac{\lambda_D^2/2Q}{\ell_K^{(PS)}} = \frac{\pi \left(\varepsilon k_B T\right)^2}{n_q e^4 \ell_K^{(PS)}} = 0.0132,$$

a negligible increase. Here, $\lambda_D = \sqrt{\varepsilon k_B T/2n_q e^2}$ is the Debye length, $Q = e^2/4\pi\varepsilon k_B T$ is the Bjerrum length, and e is the elementary charge. We used a permittivity, $\varepsilon = 35\varepsilon_0$, roughly between that of water and dry polystyrene.

Taking the steric and dielectric effects into account, C_∞ for PVBTMA should be within the range of 9.85 to 13.4 or slightly higher. We experimented with values in this range and found no significant effect on the resulting $\phi\left(\zeta\right)$ profiles. This insensitivity suggests that polymer stretching effects play a minor role in our system. This is further corroborated by the results, Chapter 4, where we use $C_\infty = 9.85$ as in polystyrene, with the understanding that the calculation may overestimate stretching effects. Similar to polystyrene, a Kuhn segment of PVBTMA is 1.86 nm long and 7.38 monomers. Each chain has 160 repeat units of PVBTMA, and therefore 22 Kuhn steps steps.

An important quantity for the Scheutjens-Fleer calculation is the number of water molecules displaced by a Kuhn segment. The chain is composed of 83% [PVBTMA][Br$^-$], a single repeat unit of which displaces 0.265 nm^3. The remainder is poly(4-methylstyrene),

which displaces $0.193\,\text{nm}^3$ [62]. Therefore, $V_K = 1.87\,\text{nm}^3$, and $V_K/V_{H_2O} = 63$; that is, each Kuhn segment displaces 63 water molecules. Because $V_K/V_{H_2O} \gg 1$, any non-uniformity in the polymer chemical potential is strongly penalized; for each polymer segment available to take a random step, there are 63 water molecules available to level gradients in chemical potential.

3.3   Chain areal density, σ

X-ray scattering of the PMB-PVBTMA membrane is used to calculate the grafting density as a function of water activity, $\sigma(a)$, needed for equation 2.11. The grafting density depends on water activity: unlike in a traditional surface-grafted polymer brush, the chains have the freedom to spread laterally, at the expense of added surface energy [63]. To compute σ, one must know the layer width for both PMB and PVBTMA. The combined width is straightforward to measure using small-angle x-ray scattering (SAXS), where it is known as the lamellar repeat spacing, d. It is determined from the wave number at the primary peak, $q*$, as $d = 2\pi/q*$. These measurements were performed on the membrane sample at the Advanced Photon Source at Argonne National Laboratory. Azimuthally averaged scattering intensity profiles are shown in Figure 3.2(a) for the five humidity levels sampled [1]. Fitting the data with a 3rd-order Hermite interpolation determined $q*$ to within about 0.04%, but the broad peak indicates that there is variation in d-spacing across the sample. Nonetheless, a change in $q*$ is sufficient to determine the change in d-spacing, shown in Figure 3.2(b), given that the peaks do not change shape. It begins at $38.9\,\text{nm}$ for the dry membrane, then drops down slightly and remains lower for the next three humidity steps. All the while, the membrane is swelling with water, indicating that the swelling is predominantly by decreasing σ [63]. In the last humidity step, d increases to $42.8\,\text{nm}$, predominantly through widening of the PVBTMA block.
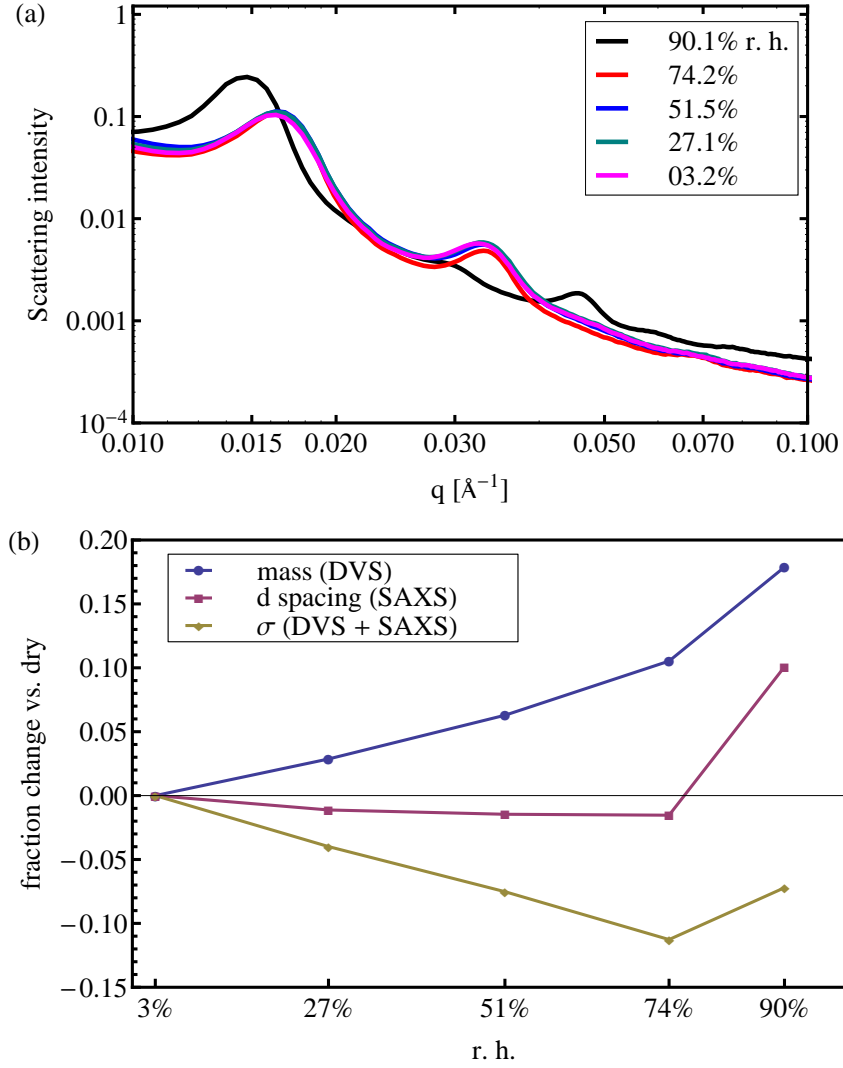
Figure 3.2. (a) Log-log plot of scattering intensity vs. wave vector, q, showing peaks characteristic of lamellar structure [1]. The smallest q peak for each water activity is used to calculate the lamellar repeat length, $d = 2\pi/q$. (b) This d-spacing (middle curve), combined with DVS mass uptake of the membrane sample (top curve), gives the grafting density, σ, (bottom curve) versus relative humidity using equation 3.1. The linear interpolation of σ is needed in equation 2.11.

To determine the proportion of the lamellar spacing occupied by each block, one possible method is to fit the scattering profiles to simulated scattering curves. With only a few discernible peaks in the data, however, we were unable to get accurate results.

Instead, mass uptake can be used to determine the block-width ratio. A dynamic vapor sorption (DVS) run was performed using the same membrane as in the SAXS experiment, under identical conditions and humidity stepping protocol. The DVS determined how much water was absorbed after each humidity step. Assuming ideal mixing of PVBTMA and water, this determines the swelling of the PVBTMA layer. Consider a single polymer in the membrane. Let v_1 ($48.7\,\mathrm{nm}^3$) be the volume of its PMB block; v_2 ($40.6\,\mathrm{nm}^3$) be the volume of its PVBTMA block., and v_w be the average volume of water per chain in the membrane, as measured from DVS. Then the total volume per chain is $v_{\mathrm{tot}} = v_1 + v_2 + v_w$. This quantity can also be expressed as $v_{\mathrm{tot}} = \sigma^{-1} d/2$, since σ^{-1} is the average interfacial area per chain. Combining these two expressions,

$$\sigma = (d/2)(v_1 + v_2 + v_w)^{-1}. \tag{3.1}$$

The normalization constant, $\sigma V_K / \ell_K$, is derived from the values in Table 3.1 for the five water activities studied in the SAXS experiment. The values remain within a narrow range of 0.194 to 0.219. Nevertheless, we include this variation in the brush calculation by defining the function $\sigma(a)$ as the linear interpolation of the measured values (see figure 3.2). That is, the water activity determined by the brush profile via equation 2.12 must equal the water activity used to determine $\sigma(a)$ in equation 2.11. This additional requirement for self-consistency can be incorporated by using $\phi_{\mathrm{avg}}(m)$ to calculate a (equation 2.12), and then using that a to interpolate σ for use in equation 2.11.

The grafting densities inferred in Table 3.1 can be cross-checked by the following rough analysis. The grafting density varies in such a way as to minimize the total energy of the

28

a	0.032	0.271	0.515	0.742	0.901
d (nm)	38.9	38.4	38.3	38.3	42.8
v_w (nm^3)	0.354	3.03	6.23	10.2	17.1
σ (nm^{-2})	0.217	0.208	0.200	0.192	0.201
$\sigma V_K/\ell_K$	0.219	0.210	0.202	0.194	0.203

Table 3.1: Quantities inferred from scattering and DVS experiments as inputs to brush calculation. The dimensionless quantity $\sigma V_K/\ell_K$, grafting density times Kuhn segment volume by length, is the prefactor required in equation 2.11. The other columns from top to bottom are: lamellar spacing, d, measured from SAXS; volume of absorbed water per chain v_w, determined from DVS; and grafting density, σ, determined from equation 3.1.
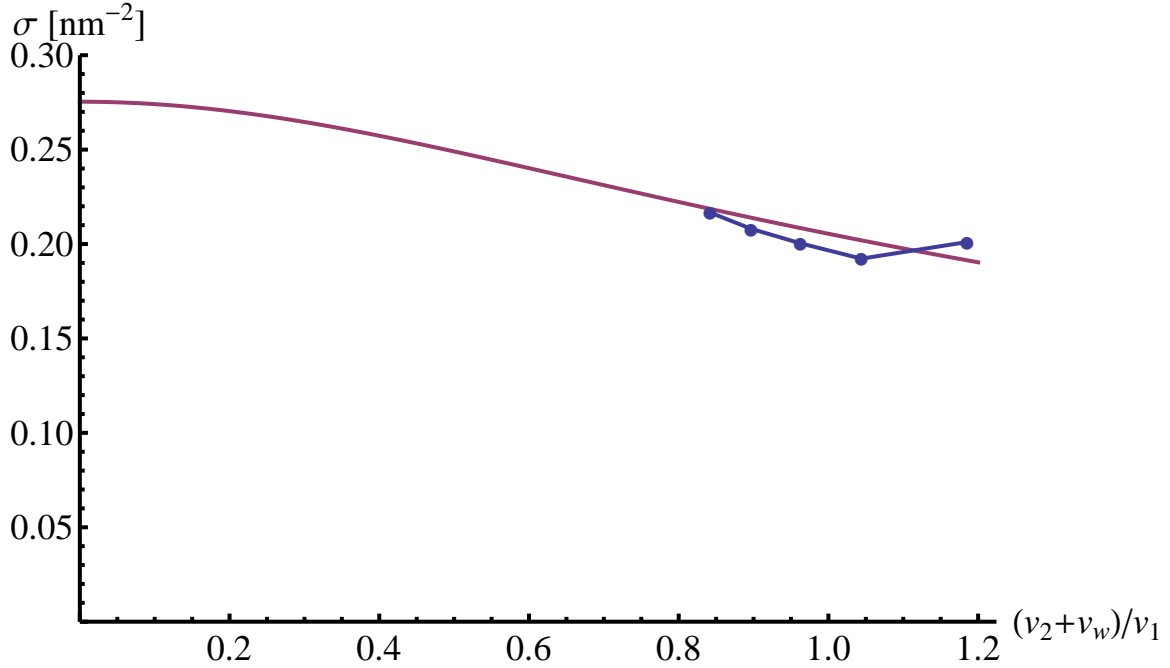
Figure 3.3. Grafting density, σ, versus swelled hydrophilic-to-hydrophobic block volume ratio, $(v_2 + v_w)/v_1$. The analytic scaling curve (equation 3.2) roughly matches the first four data points (Table 3.1), but does not capture the uptick in the last point.

system. The surface tension of the hydrophilic/hydrophobic interface, γ, acts to minimize the surface area σ^{-1}. The surface energy per chain is given by $U_S = \gamma\sigma^{-1}$. We neglect any dependence of γ on water uptake. The entropy due to stretching of each block acts to minimize the width of its respective lamella. Let U_1 and U_2 be the stretching energy per chain of the hydrophobic block and hydrophilic block, respectively. Then

$$U_i = \frac{k_B T}{2} \frac{(\eta v_i \sigma)^2}{\langle r^2 \rangle_{0i}},$$

where the subscript i takes value 1 for the hydrophobic block and 2 for the hydrophilic block. Here we have assumed that the average end-to-end distance of the chains can be written $(\eta v_i \sigma)$, where $(v_i \sigma)$ is the lamellar width and η is a fixed proportionality constant. The total free energy is $F = U_S + U_1 + U_2$. The condition for a minimum in free energy is $F'(\sigma) = 0$. This results in a scaling law,

$$\sigma \propto \left(\langle r^2 \rangle_{0,2} v_1^2 + \langle r^2 \rangle_{0,1} (v_2 + v_w)^2 \right)^{-1/3}. \tag{3.2}$$

The number of repeat units per chain are $n_{b,1} = 358$ and $n_{b,2} = 160$ for PMB and PVBTMA, respectively. The characteristic ratio for PMB is $C_{\infty,1} = 7.2$ [59], and for PVBTMA is $C_{\infty,2} \approx 9.85$ as discussed in Section 3.2. The bond length, ℓ_b, should be the same for each. Taken together, this gives:

$$\frac{\langle r^2 \rangle_{0,2}}{\langle r_0^2 \rangle_{0,1}} = \frac{C_{\infty,2} n_{b,2} \ell_b^2}{C_{\infty,1} n_{b,1} \ell_b^2} = 0.61.$$

Figure 3.3 shows how the scaling law fits the measured grafting densities from Table 3.1. The scaling law follows the downward trend in the points, until the last point which ticks up. This trend has also been measured in other experiments [63]. It is likely due to another

force becoming relevant, possibly due to geometric constraints preventing the lamellae from swelling laterally past a certain point.

3.4 PVBTMA water absorption vs. a

To account for the interaction between water and PVBTMA in solution, the model requires the chemical potential $\mu_K(\phi)$ of the loose hydrophilic polymer (i.e. just PVBTMA with free ends). This requirement was simplified in Section 2.4 to finding the chemical potential of water, μ_w, in such a sample. We explain the process of determining $\mu_K(\phi)$ in the following sections: Section 3.4.1 describes the dynamic vapor soprtion experiment, which measures the total swelled mass, M, of the sample as a function of water activity, a. Section 3.4.2 introduces a phenomenological function used to interpolate and extrapolate $\mu_w(\phi)$ based on generalizing the Flory-Huggins expression to arbitrary polynomial order. Section 3.4.3 details how $\mu_w(\phi)$ is transformed to the experimental variables and fit to the data, and the model selection process. Section 3.4.4 highlights three fits that are supported by the data, two of which are nearly identical and indicate that the sample is insoluble below $\phi \approx 0.5$. The other fit indicates a phase separation between two phases, $\phi = 0.23$ and $\phi = 0.81$. Both of these possibilities are explored in the Scheutjens-Fleer calculation in Chapter 4.

3.4.1 Experimental measurement of $a(M)$

A dynamic vapor sorption (DVS) apparatus, DVS Advantage (Surface Measurement Systems Ltd.) was used [1] to measure the mass, M, of the swelled PVBTMA sample at controlled temperature, $T = 60°C$, and water activity, a. This gives the activity of the sample as a function of its total mass, or $a(M)$, (see Figure 3.4).

Water soluble hydrophilic block samples were dissolved in water at approximately 40%
by weight and pipetted onto the surface of the sample tray. The diblock membrane samples
were cut to approximately $2\,\text{mm} \times 2\,\text{mm}$ and placed on the tray. The DVS experiment was
conducted at a constant temperature $(60°\text{C})$ and varied humidity set points. The water
soluble sample experiments starts with 6 hours of dry nitrogen flow to remove the initial
water followed by a sequence of 2 hour humidity steps with the humidity increasing by
10% each step. The sequence completes with a 2 hour step at 95% relative humidity.

Due to differences in synthesizing the PVBTMA in the membrane vs. stand-alone,
the polymers are slightly different. The polymer used in this section is in chloride form
(random 84% by mole PVBTMA$[\text{Cl}^-]$, 16% P4MS), with degree of polymerization 277.
To be consistent despite these differences, we deal with $\mu_w(\phi)$, the chemical potential per
water molecule in solution with polymer at volume fraction ϕ. Non-dimensionalizing in
this way allows the halides to be interchangeable (see Section 7.1).

3.4.2   *Generalized Flory-Huggins* $\mu_w(\phi)$

We need a parametrized phenomenological function to interpolate the DVS data that cap-
tures the required behavior in the $\phi \to 1$ limit as well as the $\phi \to 0$ limit, which our DVS
data do not access. The following generalized Flory-Huggins [64] has the proper limiting
behavior and fits the data well:

$$\mu_w(\phi)/(k_B T) = \log(1-\phi) + \sum_{i=1}^{D} c_i \phi^i. \tag{3.3}$$

In the canonical formulation [65,66] with uncharged polymers, $D = 2$, c_2 is called χ,
and $c_1 = 1 - r^{-1}$, where r is the volume ratio of a PVBTMA block to a solvent molecule
(here $r = 63 \cdot 24 \gg 1$). The deviation of c_1 from unity is due to the polymer's center-of-mass
translational entropy. We ignore this effect, since it is tiny in the loose polymer sample and

32

absent in the membrane. Polyelectrolytes, however, have another source of entropy from dissociated counter-ions, an effect which can be estimated. The Bjerrum length, Q, for the polymer is calculated to be $Q = 0.752\,\text{nm}$, [2] while the average charge spacing along the backbone, A, is calculated to be $A = 0.211\,\text{nm}$. [3] The ratio $Q/A = 3.55 > 1$, which means charge screening dominates, thus inducing counter-ion condensation and increasing the distance between uncondensed ions from A to approximately Q [68]. Therefore, in dilute mixtures, $\mu_w(\phi)/(k_B T) \approx -(A/2Q)(\phi/V_m)V_{H_2O} \approx -0.0166\phi$, where $V_m \approx 0.254\,\text{nm}^3$ and $V_{H_2O} = 0.0299\,\text{nm}^3$ are the average volume of a monomer and of a water molecule, respectively [69]. This fixes $c_1 = 0.9834$. Although the calculation leading to this value is only a rough estimate, it shows that c_1 cannot deviate far from unity. The higher-order coefficients are determined by fitting.

3.4.3   Fitting $\mu_w(\phi)$ to $a(M)$

Equation 3.3 gives $\mu_w(\phi)$, but the DVS data is of the form $a(M)$. Therefore, we need to find $\phi(M)$ and $\mu_w(a)$, and perform least-squares fitting using the function $a(\mu_w(\phi(M)))$. Finding $\phi(M)$ requires the density of water, $\rho_w = 1.00\,\text{g/cm}^3$, and that of the hydrophilic polymer in chlorinated form at 83.9% functionalization, estimated as $\rho_p = 1.29\,\text{g/cm}^3$. The dry polymer mass, M_p, becomes a fitting parameter. Assuming ideal mixture,

$$\phi(M) = \left(M_p/\rho_p\right)/\left(M_p/\rho_p + \left(M - M_p\right)/\rho_w\right), \tag{3.4}$$

since the absorbed water mass is $\left(M - M_p\right)$. The second relation, $a(\mu_w)$, is found from assuming ideal gas, which is a good approximation at ambient pressure: $\mu_w = k_B T \log a$.

---

2. $Q = e^2/4\pi\varepsilon k_B T$. For water at 60°C, $\varepsilon = 66.74\varepsilon_0$. [67]

3. $A = (2\ell_b \sin \ell_b/2)(\%\text{Cl})$, where $\%\text{Cl} = 0.839$ is the fraction of monomers with a chloride.

D	M_p	c_2	c_3	c_4	c_5	c_6	RSS	ΔAIC_c	$\mathscr{L}$
2	16.9886	0.801	0	0	0	0	0.42212	160.8	0.00%
3	16.8640	4.395	-4.417	0	0	0	0.04626	63.8	0.00
4	16.8113	-12.77	37.68	-25.76	0	0	0.01411	13.1	0.12
5	16.7011	99.56	-375.3	479.7	-206.1	0	0.00991	0.0	81.1
6	16.7086	183.3	-782.7	1222.	-806.5	181.8	0.00990	2.93	18.7

Table 3.2: Best-fit parameters to the DVS data, using equation 3.3. D is the polynomial degree, M_p the dry polymer mass, and c_i the polynomial coefficients. The 2nd-order fit corresponds to the canonical Flory-Huggins formula with $\chi = c_2$. As expected, the residual sum of squares, RSS, decreases with increasing order. The AIC_c value is smallest for $D = 5$, indicating that it is the best model of the data. ΔAIC_c is the increase in AIC_c compared to $D = 5$. These provide an estimate for the likelihood, $\mathscr{L}$, of each model: $D = 5$ is the highest, followed by $D = 6$ and $D = 4$, with negligible support for $D = 2$ or $D = 3$.

Figure 3.4 shows the least-squares fits for $D = 2$ through $D = 6$, and Table 3.2 lists their parameters, $\{M_p, c_2, \ldots, c_D\}$. Except for the $D = 2$ fit, the curves qualitatively follow the data and improve with increasing D, until $D = 6$ which practically overlaps with $D = 5$. This is not surprising since the set of functions of order D is a superset of the functions of order $D - 1$. Without care, however, this can lead to over-fitting the data. We use the corrected Akaike Information Criterion, or AIC_c, to compare best fits of each order. The AIC_c is given by: $J \log RSS/J + 2K + 2K(K+1)/(J-K-1)$, where $J = 45$ is the number of data points, and $K = D + 1$ is the number of model parameters (i.e., $\{M_p, c_2, \ldots, c_D\}$ plus σ^2, the estimated variance). Only differences in AIC_c matter. The model with the lowest AIC_c, in this case $D = 5$, is the likeliest. The difference, ΔAIC_c, between a given model's AIC_c and the smallest AIC_c determines the model's relative likelihood, which is given by $\exp(-\Delta AIC_c/2)$ [70]. Table 3.2 shows the RSS, ΔAIC_c, and normalized likelihood, $\mathscr{L}$, for each of the models considered. The highest likelihood is for $D = 5$ at 81.1%, followed by $D = 6$ at 18.7%, and $D = 4$ at 0.12%. $D = 2$ and $D = 3$ are ruled out, with negligible likelihood ($< 10^{-13}$). We stopped at $D = 6$ since AIC_c will continue to rise thereafter, indicating over-fitting.
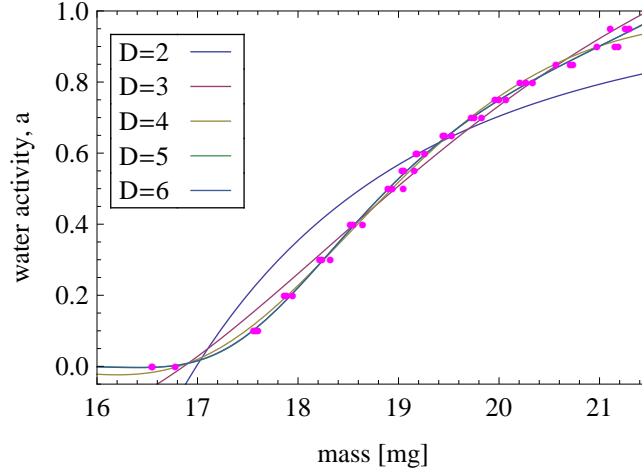
Figure 3.4. Water activity, a, vs. mass, M, of untethered PVBTMA sample, with phenomenological fitting functions. Points are measured as described in Section 3.4. Curves are calculated using equation 3.3, with equation 3.4 used to convert between ϕ and mass. The curves from top to bottom above mass = 17.5 mg correspond to polynomial degree $D = 2$, 3, 4, 5, and 6, respectively. The fitting improves up until order $D = 5$, at which point the curve has essentially converged.

3.4.4 Two distinct models, $D = 4$ and $D = 5$

It turns out that the fit for $D = 4$ differs significantly from $D = 5$ and $D = 6$, despite all three being close fits to the DVS data. This is largely due to the difference in fitted M_p, to which the model is very sensitive, since it shifts the position of the logarithmic divergence in μ_w. Also, there is no data below about $\phi = 0.74$, so the models must extrapolate there. The discrepancy between the different fits can be seen in plots of their Helmholtz free energy per lattice cell, A/N, vs. ϕ (see Figure 3.5), found by integrating equation 2.13. In regions where the curve is purely convex, such as at high ϕ, the two components form a stable, uniform mixture. Where the curve is concave, the system prefers to follow the common tangent line (dashed), e.g. the line connecting two points $(\phi_X, A(\phi_X))$ and $(\phi_Y, A(\phi_Y))$ where $A'(\phi_X) = A'(\phi_Y)$. These two conditions are equivalent to $\mu_w(\phi_X) = \mu_w(\phi_Y)$ and $\mu_p(\phi_X) = \mu_p(\phi_Y)$, meaning that solutions at ϕ_X and ϕ_Y coexist stably. A point along the common tangent line signifies that the sample is phase-separated, with part at ϕ_X and part

at ϕ_Y [56]. For future reference, one should consider using this modified form of the curve to perform the least-squares fitting, especially if the sample is observed to phase separate. Otherwise, a fit could imply a solubility gap where none is seen in the data. We used the unmodified curve, which is suitable if the sample enters the metastable region, a possibility we could not rule out. This ambiguity is only an issue for the $D = 4$ fit.

Figure 3.5 shows that even though the fit for $D = 4$ approximates the DVS data reasonably well, it suffers from the inconsistency mentioned in the previous paragraph. According to the fit, the sample should phase separate between $\phi = 0.23$ and $\phi = 0.81$. The data, though, seem to exclude the top of this range since measurements were taken as low as $\phi = 0.74$. It is possible, though, that the mixture was either in a metastable state or barely phase separated – its appearance changed from matte to glossy. Therefore, we can not rule out the $D = 4$. Unfortunately, standard DVS protocol is to halt the experiment at the first signs of phase separation to avoid flooding the tray. For future experiments, we would recommend carefully determining the composition of the coexisting phases. Even if the $D = 4$ suffers from some inconsistencies, it makes for a good contrasting example to the other two.

Figure 3.5 shows that the fits $D = 5$ and $D = 6$ are thermodynamically practically identical to one another. They form a single-phase solution between $\phi = 0.72$ and $\phi = 1$, dry polymer. There is a solubility gap below $\phi = 0.72$, as indicated by the dashed line. The gap extends down to a stable phase of ultra-pure water, $\phi \approx 0.$ [4], where the curve dips below zero before turning back to intersect the origin (not visible). The DVS did not probe below about $\phi = 0.74$, since the sample showed signs of phase separation. This is consistent with the phase separation predicted by the $D = 5$ and $D = 6$ models. In addition, a slightly al-

---

4. $\phi \approx 10^{-506}$. $A(\phi) = 0$ when $(1 - c_1) \log \phi = 1 - \sum_{i=2}^{D} c_i (i-1)^{-1}$.

tered sample with fewer ionic groups showed strong immiscibilitiy, in agreement with our $D = 5$ behavior. Evidently, our sample is very near the boundary between the two behavior.

It is worthwhile to study both solvent types. The next step is to calculate the chemical potential curves, shown in Figure 3.6. The curves for water, μ_w, are calculated via Section 3.4.3, and curves for solvent, μ_s, via equation 2.15. These curves provide a different way of understanding the distinction between $D = 4$ and $D = 5$. The curvature of μ_w at $\phi = 0$ tells whether a dilute mixture is thermodynamically possible. For $D = 4$, $\mu_w''(0) < 0$, so the $D = 4$ fit represents a good solvent in this limit. Conversely, for $D = 5$, $\mu_w''(0) \gg 0$, so the $D = 5$ fit represents a very poor solvent that does not mix at small, finite concentrations. The two models disagree so flagrantly in this limit because all the measurements were taken for concentrated mixtures. For clarity, each data point shown is the average over the three runs. The data are plotted twice; once for the dry polymer mass M_p found from the $D = 4$ fit and again for the M_p found from the $D = 5$ fit. The two μ_s curves agree reasonably well up to a constant in the region where data is available, but disagree for lower ϕ. Chapter 4 shows that the two models result in different swelling predictions in the regions where μ_s is extrapolated outside the range of the data.
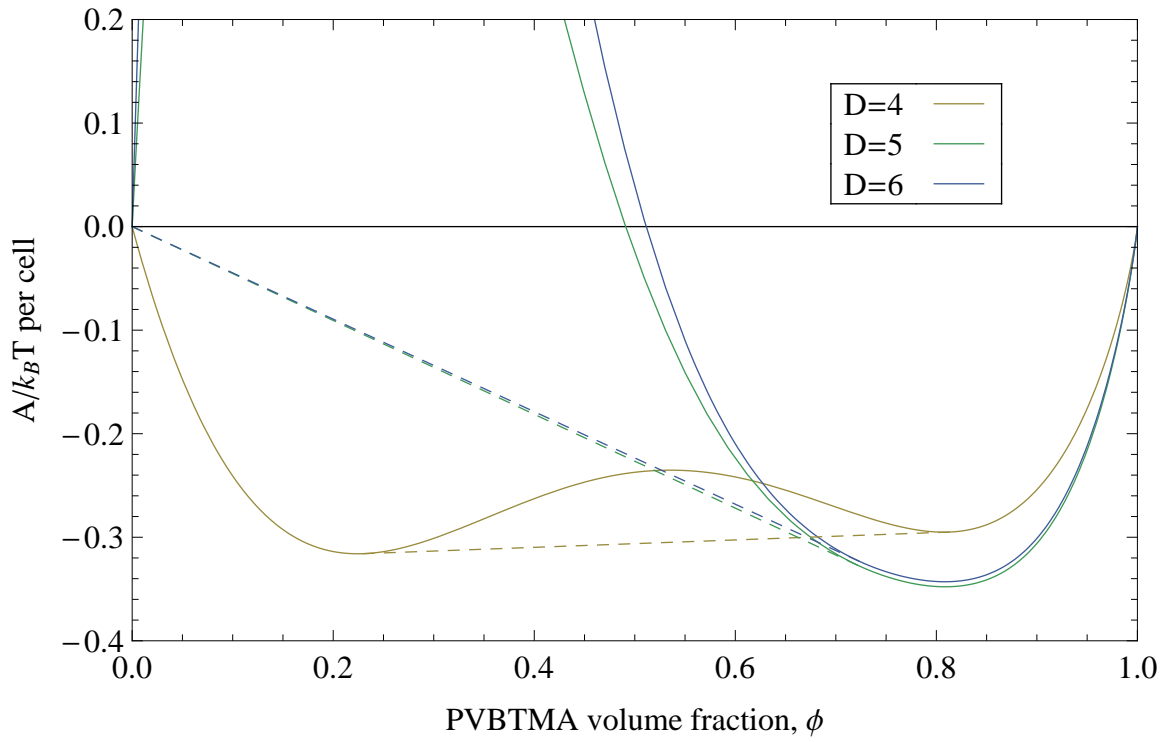
Figure 3.5. Average free energy of the PVBTMA-water solution per lattice site, A/Nk_BT, for the Flory-Huggins fits (equation 3.3) for polynomial degree 4, 5, and 6. The dashed line shows the mutual tangent line, which describes the phase separation.
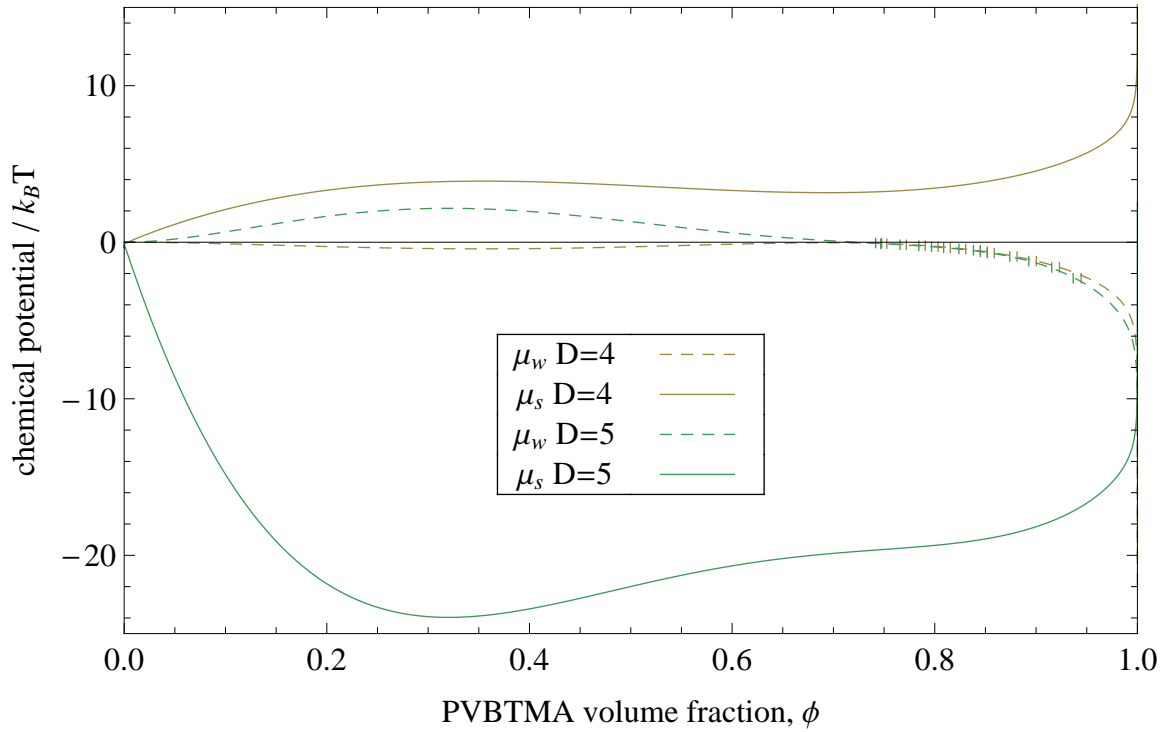
Figure 3.6. Plots of μ_w and μ_s (equation 2.15) for the $D=4$ fit and $D=5$ fit. The DVS data, averaged across runs, are plotted as vertical ticks. The data are plotted once for the M_p found by the $D=4$ model and again for the M_p found by the $D=5$ model. The μ_w (dashed, $D=4$ below, $D=5$ above) are fit according to Section 3.4.3. The resulting μ_s curves (solid, $D=4$ top, $D=5$ bottom), used in the Scheutjens-Fleer calculation, agree up to a constant in the range where data is available but disagree elsewhere.

CHAPTER 4

CALCULATION RESULTS

Using the experimental parameters found in Chapter 3, this section shows the resulting predictions of polymer/water concentration profiles within the lamellae using the Scheutjens-Fleer methodology. Section 4.1 gives the results for the $D = 5$ model, which did not lead to phase separation in the lamella profile prediction. Section 4.2 gives the results for the $D = 4$ model, which does lead to predictions of phase separation, with watery channel block in the center of the lamella.

Evidently, in the model PVBTMA polymers studied here, solvation effects dominate over chain stretching. This is due to the fact that $(V_K/V_{H2O}) \gg 1$, the volume of a PVBTMA Kuhn segment is much larger than the volume of a water molecule. This ratio appears as a prefactor in the definition of μ_K (equation 2.16), which in turn is in the exponential in the segment Boltzmann factor (equation 2.6). Therefore, the profiles are biased toward being locally flat. This flatness was observed in our calculated $\phi(\zeta)$ profiles. For a typical case, ϕ only varies about 0.01% from one Kuhn-length layer to the next. Another contributing factor to the flatness is the fact that the brushes on either side of the lamella overlap significantly compared to the length of a chain, giving the chains the opportunity to thoroughly cover the entire lamella. For example, of 10000 chain configurations sampled at $a = 0.58$, 31.5% reached or crossed the center plane. The exception to the flatness occurs when the PVBTMA and water solution is expected to phase separate, as is the case for the $D = 4$ model.

In order to find all possible self-consistent solutions, for each brush spacing, m, several starting profiles were attempted including a flat profile, and water channels of varying widths. Also, to discourage the algorithm from skipping over solutions, the step size was limited so that for any ζ, the change in $\phi(\zeta)$ per iteration was less than 0.02. Some initial

guesses never converge; these runs were discarded. For calculations that did converge to a self-consistent profile, we calculated the resulting water activity (equation 2.12) and free energy per chain (equation 2.17). These points are connected to show how the membrane swells versus water activity.

In each section, the predicted swelled brush width, w, is compared to experiment. These values are inferred by combining the SAXS d-spacing with the DVS mass uptake, similar to the calculation of σ in Section 3.3. The brush width, w, is the average width of a hydrophilic block, i.e., half the total hydrophilic lamellar spacing. It equals the swelled volume of a hydrophilic block, $v_2 + v_w$, divided by the average interfacial area per chain, σ^{-1} :

$$w \;=\; (v_2 + v_w)\,\sigma = \frac{(v_2 + v_w)\,d}{2\,(v_1 + v_2 + v_w)}. \tag{4.1}$$

This forms an independent cross-check, since two independent experimental measurements, v_w and d, were collected at each water activity, but only one combination of them, σ, was previously used. Between $a = 0.03$ and $a = 0.90$, the brush width increases from $8.88\,\mathrm{nm}$ to $11.60\,\mathrm{nm}$, or $4.78\ell_K$ to $6.24\ell_K$. This does not afford much resolution in the calculation, which is limited to increments of $0.5\ell_K$ in brush width. Therefore, in the following sections we quadrupled the chain molecular weight to $n = 88$. The reported lengths are scaled by $1/4$, so that the effective spatial resolution is $\ell_K/4 = 0.465\,\mathrm{nm}$. This is an established way to scale the resolution [45], but it has the side effect of giving the chains more stretching entropy. This is moot in our case since the scaled system is still within the regime of negligible stretching energy, so it does not significantly affect the results.

Both models are in quantitative agreement with the experiment, with the $D = 5$ model giving a slightly better prediction of swelling. No experimental evidence of water channels is seen, but their presence cannot be ruled out. Sources of experimental error include: polydispersity in the polymers used, inhomogeneity within the membrane, uncertainty in

humidity measurements especially at high humidity, assumptions made in extracting the swelling width such as ideal mixing, and using the chlorinated and brominated form of the polymer interchangeably (see Section 7.1). Sources of error in the calculation include: ignoring effects smaller than a Kuhn length, ignoring dipole effect due to non-uniformity (see Section 7.4), uncertainty in fitting the DVS data, not having a measurement of the characteristic ratio, and ignoring interaction with the hydrophobic layers other than setting the grafting density.

4.1   Without phase separation ($D = 5$)

This section uses the best overall fit to the DVS data, i.e. equation 3.3 with $D = 5$ and the parameters given by Table 3.2. This model predicts that untethered PVBTMA is not soluble in water below $\phi = 0.722$ (Figure 3.5). Figure 4.1(a) shows the shapes of the profiles as the water activity is increased from 0 to 1. From dry to water activity $a = 0.759$, the lamella swells gradually, expanding in width by only 3 Kuhn lengths (there are only four profiles spanning this humidity range). Above $a = 0.759$, the lamella swells linearly with increasing a, but at a faster rate. The two swelling rates can be seen in Figure 4.1(b), where each circle point corresponds to one profile, with matching color. The transition point, $a = 0.759$, between the two swelling rates corresponds to the minimum in grafting density (Figure 3.2b). Below this point, σ decreases with a, tending to counteract the swelling. Above it, σ increases with a, enhancing the swelling. The calculation predicts a water channel forms at $w = 11.6\,\text{nm}$ and $a = 1.0$. After that point, the lamella swells solely from a increase in the water channel width; the profile maintains a fixed shape. Figure 4.2 shows that the water channel width grows 1-to-1 with lamella width.

Compared to the swelling inferred from combined SAXS and DVS in equation 4.1 (Figure 4.1(b) black squares), the predicted swelling agrees to within about 10%, which
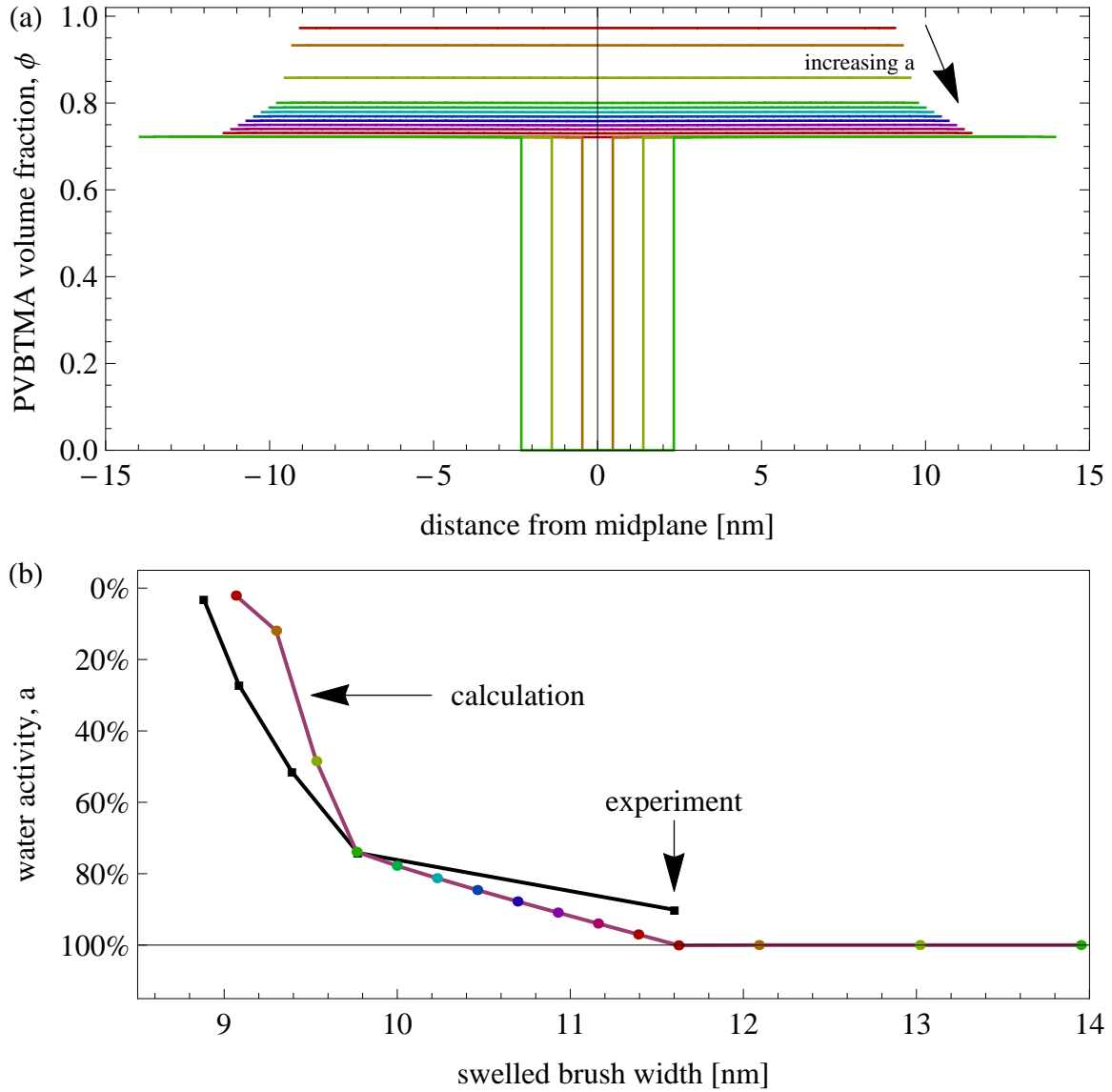
Figure 4.1. (a) The predicted polymer distributions within the hydrophilic lamella at different lamellar widths, using the $D = 5$ DVS fit. The width is given by the horizontal extent of each graph; on either side of each profile is a hydrophobic layer (not shown). All the profiles are extremely flat locally. Channels of pure water form at widest spreads. (b) The water activity of each profile is calculated from equation 2.12 and plotted versus brush width with a point of the same color. Below $a = 100\%$, the calculation predicts two swelling rates, in agreement with the SAXS and DVS combination (equation 4.1, black squares). All profiles with brush width greater than 11.6 nm have a water channel and are at $a = 100\%$. This width also corresponds to the largest width measured in humid air.

43

was roughly the accuracy of the parameters fed into the calculation. The prediction some-what over-predicts swelling for $a < 0.759$ and under-predicts the swelling for $a > 0.759$. Nevertheless, the good agreement supports the case that water is distributed very uniformly within the lamellae.

The model predicts that the free energy bottoms out at a lamellar width of 23.3 nm. Self-consistent profiles continue to be possible above this width, but as Figure 4.3 shows, the free energy does not vary beyond this point. The profiles remain the same shape, just with added water in the center. Therefore, any swelling beyond this point is due to forces not considered by our calculation. In addition to the swelling data in Figure 4.1(b), an-other measurement was performed at $a = 1.0$. Dr. Tsai soaked the membrane in water for 24 hours and reports the following changes compared to the dry membrane: the d-spacing increases from 41.9 nm to 68.8 nm, while the mass uptake divided by the dry mass, $(M - M_p)/M_p$, was 1.728 [1]. Using equation 4.1 with v_1 and v_2 from Section 3.3 and the block molecular weights from Section 3.1, this results in a maximum hydrophilic lamellar width, $2w$, equal to 56.3 nm. Therefore, the $D = 5$ model says that water channels should have been present in the soaked membrane, and that forces external to the PVBTMA layers caused the membrane to swell to that point.

Overall, the predictions match the experimental cross checks to within about 10–20% and capture the qualitative features of the data.

4.2   With phase separation ($D = 4$)

This section uses the best fit generalized Flory-Huggins equation of state (3.3) with $D = 4$, with the parameters given in Table 3.2. This model predicts that untethered PVBTMA has a solubility gap in water between concentrations $\phi = 0.230$ and $\phi = 0.813$ (Figure 3.5).
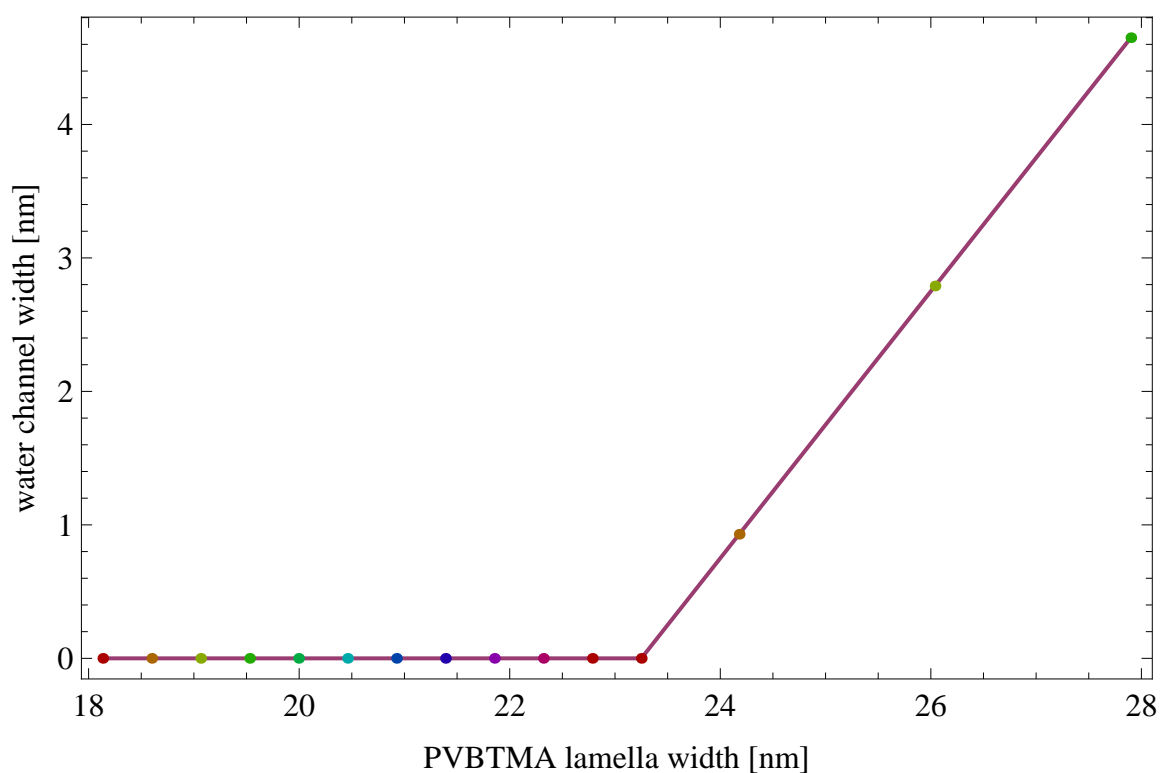
Figure 4.2. Predicted water channel width vs. PVBTMA lamella width for the $D = 5$ fit. No water channel forms until the lamellar width, $2w$, is 23.3 nm. Above that width, the profile swells solely due to the water channel expansion, and the slope is 1.
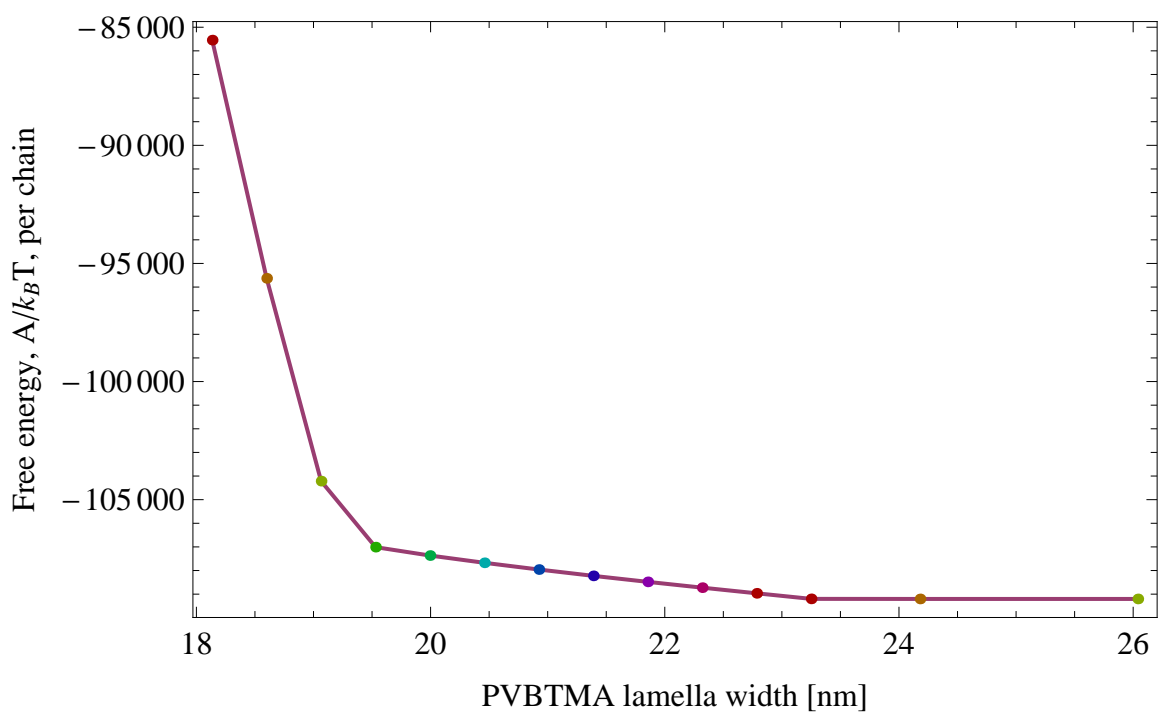
Figure 4.3. Total Helmholtz free energy of the system, A, per chain compared to pure water (equation 2.17) versus the PVBTMA lamella width. The free energy drops as the swelling increases, up to 23.3 nm. Additional swelling occurs solely from water channel expansion, which costs no free energy in our model, and the curve bottoms out. This suggests the actual water channel width is set by forces not considered in the calculation.
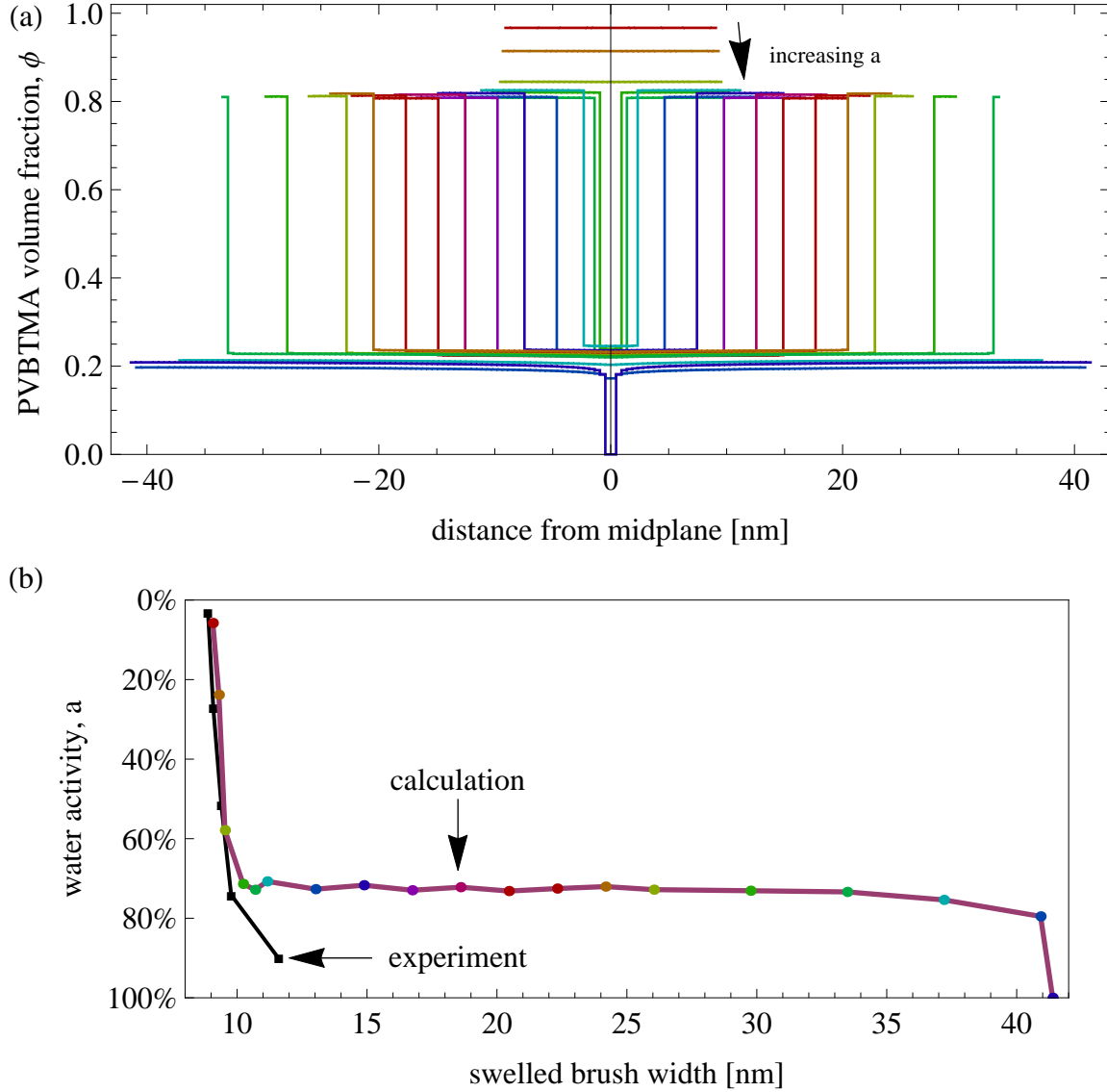
Figure 4.4. (a) Profiles for the $D = 4$ DVS fit. See Figure 4.1 caption for details. The profiles are flat, except that the solubility gap causes a water channel to form for $w >$ 9.6 nm between concentrations $\phi = 0.230$ and $\phi = 0.813$. There is slight jitter around these values since the water channel width must be an integer Kuhn length. The water channel ceases when all the polymer has moved to the dilute phase. Finally, the chains are fully stretched, leaving pure water in the center. (b) Water activity versus swelled brush width. The calculation agrees with experiment up until the point where water channels form, at $a = 72.3\%$. The profiles maintain this water activity until the water channel ceases.

Figure 4.4(a) shows that water channels form when the concentration drops to the critical threshold of $\phi = 0.813$. In this flat-profile regime, the tethering does not affect the composition of the two phases, it just ensures that all the dilute phase is centered together in the lamella. Any other arrangement of the two phases would necessitate more phase boundaries or a breaking of the mirror symmetry, so it is the chain entropy that sets this geometry. The actual compositions of the two phases varies slightly in the calculation due to discretization error, since the water channel width is artificially forced to take an integer multiple of the Kuhn length.

Figure 4.4(b) shows that the swelling predictions for $D = 4$ agree with some of the cross checks but not all. From 0% through 72.3% water activity, the predicted swelling according to this model follows quite closely to that of the $D = 5$ model, and both are in good agreement with the SAXS+DVS cross-check. These are the prediction points that correspond to flat profiles.

Above $w = 10.7$ nm, all the predicted profiles are water channel shapes. They fall within a narrow range of water activity, 0.709–0.730, until the brush width is nearly as long as fully stretched chains. This narrow range of a corresponds to the narrow range in ϕ at the center plane (equation 2.12). To maintain a constant ϕ at the center, polymer must move from the concentrated phase to the dilute phase as the lamella widens, increasing the channel width. It does by increasing the channel width by $1.38\ell_K$ on average for each increase in ℓ_K of the lamellar width (Figure 4.5 a). As mentioned, this introduces some frustration at small channel widths due to discretization (Figure 4.5 b).

The free energy, A, as a function of water activity (Figure 4.6) is qualitatively similar to the $D = 5$ model, except that the point at which it bottoms out corresponds to a narrower swelled width, $2w = 19.2$ nm. Beyond this point, at little to no free energy cost, the system can move between any of the water channel widths. This could cause a swelling spike at $a = 0.78$, but no effect like this was observed. Conversely, for the water channel to

swell larger than one Kuhn length, it would require expansion forces not considered in our calculation.
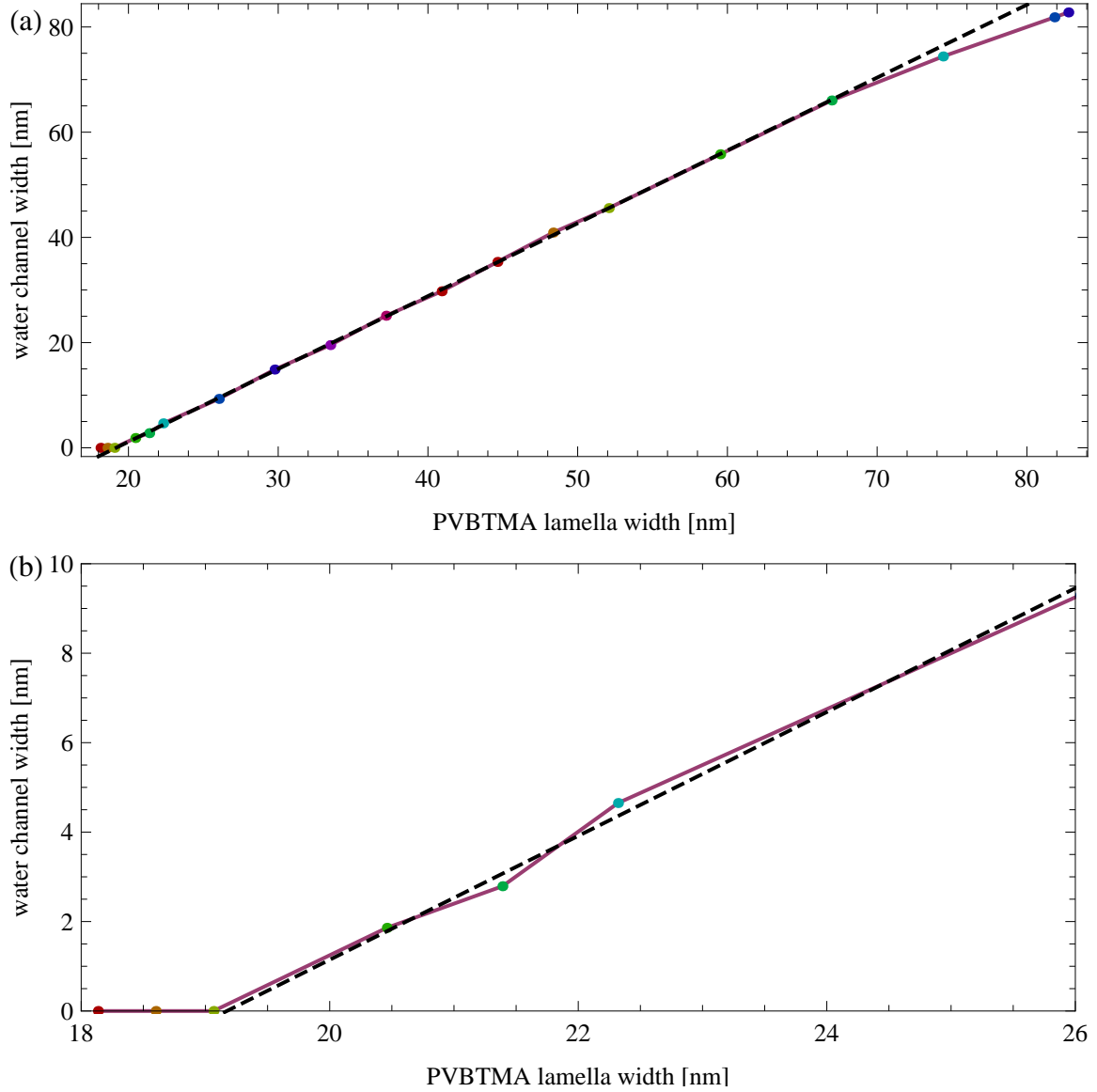
Figure 4.5. (a) Water channel width versus total PVBTMA lamella width for the profiles in Figure 4.4. A water channel forms once the PVBTMA layer width, $2w$, has grown beyond 19.2 nm. The water channel width grows as $1.38\,(2w) - 26.5$ nm (dashed line). (b) Zoomed in around the transition region, showing discretization artifacts.

Figure 4.6. Free energy per chain in units of k_BT vs. PVBTMA lamellar width for the $D = 4$ model. See Figure 4.3 for details. After a water channel forms, the free energy and water activity remain nearly constant as the lamella swells. This suggests the water channel width is set by forces not considered in this calculation.
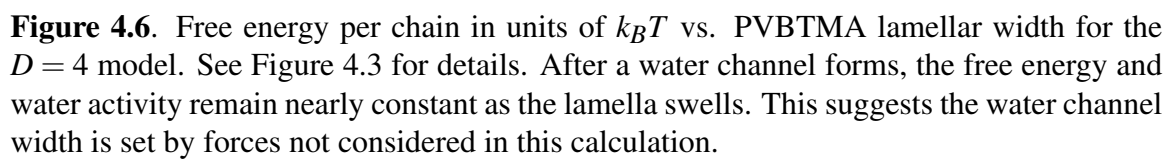
CHAPTER 5

DISCUSSION

Overall assessment   Our motivation for this research was to understand the water distribution in ion-conducting polymer membranes and hopefully find ways to improve them. The goal was to advance our understanding by using experimental measurements in places where previous theoretical studies used estimates and analytics. This approach could have resulted in simply a pragmatic advancement – a numerical validation of polymer brush theory. Instead, our results suggest a paradigm shift in the understanding of conducting blocks used in fuel cell membranes. We started with a polymer-brush mindset that the principal driver is the energy balance is between stretching and wetting. Using realistic parameters led to a different balance. First, the large Kuhn segment volume divided by solvent volume puts the polymer in a regime where stretching forces are secondary. Many of the predicted water distributions are surprisingly banal: uniform profiles whose concentration is set by the areal density, σ, itself a variable function of water activity, a. Therefore, measuring $\sigma(a)$ was critical in matching the results to experiment. Second, the realistic mixing effects between PVBTMA and water led to the surprising prediction of water channels. We showed that small changes in the mixing can lead to qualitative differences in the water concentration of the channel and to qualitatively different behavior in how the channels form and swell. There is limited evidence supporting the existence of these channels. Given their potential for increasing ion conductivity in membranes, more study on the issue is warranted.

Parameters to the model   One of the advances of this research was to incorporate rigorous experimental measurements for the model parameters where simplifications had been used in similar previous models. One of the most important parameters, and the one we

determined most carefully, was the water affinity of untethered PVBTMA. The measurements were performed to high precision using a sophisticated DVS apparatus and repeated three times. This was important, since we needed to extrapolate to more dilute concentrations than could be measured. It turned out that the extrapolation function we used, a generalization Flory-Huggins equation to polynomial degree D, was a good choice. The canonical Flory-Huggins equation, with $D = 2$, did not fit the data well, but the higher order equations did converge to the data. By eye, the $D = 4$ model fit well and we could have been forgiven for stopping there. By going to higher order, and using the AIC_c to compare models, we were able to rigorously show that the $D = 5$ model is the best fit. This turned out to be worthwhile, since the small difference in the $D = 4$ and $D = 5$ fitting resulted in a big difference in the extrapolation, and qualitative differences in the results. It should be noted that there is nothing inherently special about the numbers $D = 4$ or $D = 5$. These were simply the result of fitting our particular polyelectrolyte, and happened to illustrate two different phase behaviors. The AIC_c gave a quantitative understanding of the quality of fit, and we would recommend this methodology for fitting water uptake data. We would also recommend augmenting the water uptake data with additional data in the dilute regime, using light scattering for example.

This paper rigorously derives the Kuhn segment chemical potential, $\mu_K(\phi)$, from the chemical potential of a water molecule in the system, $\mu_w(\phi)$, taking into account the osmotic pressure. In the past, many practitioners of the Scheutjens-Fleer method have used ad hoc, idealized forms for $\mu_K(\phi)$ that did not require this derivation. The canonical Flory-Huggins equation with its symmetric interaction term, $\chi N_p N_w$, cannot capture the wetting behavior of PVBTMA and similar complex polyelectrolytes used in fuel cells.

The Kuhn length is often thought of as the natural spatial resolution of a polymer, but it also determines the linear entropy density. It was this second role that was most important in the water profile calculations. A large Kuhn-segment-to-solvent-molecule volume ratio

emphasizes mixing entropy over conformational entropy of the polymer. In this limit brush effects are muted, and water tends to be homogeneously distributed. In contrast, studies of polymer brushes have assumed solvent molecules similar in size to a monomer. Some authors even make the mistake of equating a Kuhn segment with a monomer, which vastly overemphasizes conformational entropy. Although we did not measure the Kuhn length for PVBTMA, we can safely assume that it is in this limit of large Kuhn segments. Changing the value by $\pm20\%$ turns out to have a negligible effect on the water distribution profiles. This choice in Kuhn length implies there are only 22 segments per PVBTMA block, leading to unacceptably low spatial resolution in the water profiles. Using a smaller Kuhn length to improve resolution would also alter the physics of the model. Instead, we scaled up the molecular weight of the block to 88 segments, and scaled down the reported lengths by $1/4$. This is equivalent to scaling the Kuhn length only in situations where it is used for spatial resolution, and not in computing the volume ratio. We checked that scaling in this way does not affect the profile shapes except to add more points.

In situations where the water profile is flat, the factor that governs the PVBTMA lamella width is the chain areal density, σ^{-1}. Even though σ only varies by about 10%, it was precisely this effect that enabled the predictions to quantitatively match experiment, especially at low water activity. This effect is usually not included in polymer brush swelling calculations. We included the effect as an afterthought and had to use experimental measurements of σ, diminishing the predictive power of the model. One place for improvement would be to explicitly include the hydrophobic block in the calculation via separate ϕ_{PMB} and ϕ_{PVBTMA} functions. Two interaction potentials, μ_{PMB} and μ_{PVBTMA} would be needed, and each would depend on both ϕ_{PMB} and ϕ_{PVBTMA}. The original calculation circumvented this complication by studying an A-B block copolymer with homopolymer A as the solvent [63]. It may be worth the effort in order to understand the nonlinear behavior of σ.

Another way to improve our model would be to refine the assumption of ideal mixing, used in several places of the calculation. Ideal mixing is likely to break down at high polymer concentration, and could affect the conversion from the raw DVS data to the $\mu_K(\phi)$ used in the calculation. A more realistic mixing behavior could be incorporated using experimental measurements or MD simulations. Similarly, we made assumptions in several places about the density of various forms of PVBTMA: chloride vs. bromide forms, copolymer vs. untethered, and different percentages of monomers with a charged group. It would have been less ambiguous to measure these quantities directly.

Assessment of the results   The results differ from expectations in two ways: the predicted water distributions are strikingly uniform, except in cases of phase coexistence where abrupt water channels form.

First, we discuss the flatness aspect. This prediction is surprisingly different from the broad, parabolic profiles seen in ideal polymer brushes. This is the prediction for which we have the best experimental cross-checks, with x-ray scattering and water uptake. The agreement is good, to within about 10%, which is about as much as we could hope for given the uncertainty in some of the parameters we used. Since the polymer brush stretching effect turns out to be negligible, the same result could be found without a mean-field calculation. That is, the water uptake[1] for PVBTMA in the membrane is nearly the same as the water uptake for untethered PVBTMA. These two water uptake functions should be compared, if possible, before deciding whether to study the water distribution in a polymer membrane. Their degree of dissimilarity is a proxy for the degree of inhomogeneity of water.

---

1. mass of water absorbed divided by dry PVBTMA mass, as a function of water activity

55

The second surprising prediction is that our hydrophilic polymer is not miscible at all concentrations. At certain water activity, there is a phase coexistence, and the phases arrange to form water channels. They are only predicted to form within a narrow range of water activity. If the transition occurs at $a = 1$, such as our $D = 5$ model predicts, it would be straightforward to achieve by soaking the membrane in water. If the transition occurs at lower water activity, such as our $D = 4$ model predicts, then it would require sweeping the water activity slowly while holding the temperature fixed. Experimentally measuring the water profile shape would involve sophisticated scattering techniques. Preliminary neutron scattering using a variable mixture of water and deuterated water has been performed on the PMB-b-PVBTMA membrane by Christopher L. Soles at NIST, but more work is needed. Another possibility is anomalous x-ray scattering, which isolates the scattering due to each chemical element type in the membrane.

Water channels and conductivity For any given polyelectrolyte, there is a certain non-zero concentration that maximizes ion conductivity. If there is not enough water, the ions do not diffuse. If instead there is not enough polymer, then the concentration of ions suffers. Preliminary evidence suggests this value for PVBTMA may be around $\phi = 0.2$. In unpublished MD simulations, Ying-Lung Steve Tse measured the diffusivity of fluoride ions in PVBTMA versus number of water molecules. The diffusivity rises roughly exponentially with the number of water molecules before eventually plateauing to the value for diffusivity in pure water. The point of maximum conductivity was found to be $\phi \approx 0.2$ using the Nernst-Einstein equation, which says that conductivity is approximately proportional to the product of diffusivity and ion concentration [71]. Therefore, the way to maximize conductivity with respect to water uptake is to focus the water into pathways as close to the optimal concentration as possible, in this case $\phi = 0.2$. The results for the $D = 4$ and $D = 5$ models show that there are two possibilities for water channels. In the $D = 5$ model, the channel is

practically pure water. The only way for a pure water channel to conduct significantly is by the phenomenon in Section 7.4, where ions from the concentrated phase dissociate and leak into the water phase. In the $D = 4$ model, however, the channel is at a finite concentration of $\phi \approx 0.22$. For maximizing conductivity, a polyelectrolyte with thermodynamics similar to the $D = 4$ model is probably better. In the $D = 4$ results, the water channel forms when the water activity is very close to $a = 0.82$. The fact that this activity is less than 1 is desirable, since fuel cells become flooded at high water activity. The fact that the channels only form at a specific water activity, though, is not desirable; it is unclear whether a real system could be maintained within such a narrow water activity band. One of our collaborators, Daniel M. Knauss, is exploring the idea of adding hydrophilic poly(ethylene-oxide) to the ends of the PVBTMA chains to make the water channel phenomenon more robust.

CHAPTER 6

CONCLUSION

In this paper, we used established polymer-brush theory to predict the spatial distribution of absorbed water absorbed in the hydrophilic lamellae of a diblock membrane. Under most normal operating conditions, the calculations predict a nearly uniform distribution of water. Under certain conditions, however, water is preferentially absorbed near the center plane of the hydrophilic lamella, according to our calculation. These water stripes can form if and only if a mixture of *untethered* hydrophilic block would phase separate under the same conditions. That is, two mixtures at different concentration coexist in equilibrium (both with the same chemical potentials) at the surrounding humidity level. In that case, there is no solvation energy penalty for having non-uniformities in the polymer/water ratio, as long as the disparate regions are coexisting phases. The conformational entropy generated by tethering each hydrophilic chain to an interface serves as a tie-breaker between otherwise equivalent states.

Using the methods and results from this study, it should be possible to engineer polymers that form water channels more easily. If they can be made to be robust, it provides a way to concentrate water into conducting pathways. This arrangement maximizes ion diffusivity for a given amount of water, and leaves the majority of the membrane relatively dry and strong. Water channels have recently been observed in proton-exchange membranes. The next step will be to generate them in alkaline anion exchange membranes and experiment with their properties. Hopefully this work is a step toward cost-efficient, viable alternatives to batteries and combustion engines.

CHAPTER 7

APPENDIX

7.1 Br/Cl interchangeability

The Scheutjens-Fleer method requires the solubility function of the isolated (untethered) hydrophilic block (Section 3.4). Due to differences in synthesizing the block copolymer versus the isolated hydrophilic block, the chloride form of the polymer was used for the DVS measurement whereas the bromide form was used in the membranes. The following argument shows that both forms should have nearly the same solubility when measured as water activity vs. volume fraction. Cohen et al. [2] performed very accurate water uptake experiments on droplets suspended by an electric field comparing NaCl versus NaBr. They report the data as a polynomial fit water activity vs. molality, or moles of substance per kilogram of water. To convert from molality to volume fraction, ϕ, requires the condensed density of the substance, ρ, and the molar mass, M. For example, bromine has a molar mass of $M_{Br} = 0.0799\,\text{kg/mol}$ and a condensed density of $\rho_{Br} = 3100\,\text{kg/m}^3$. Ignoring the sodium for simplicity, a solution of volume V has $V\phi_{Br}\rho_{Br}/M_{Br}$ moles of bromide, and $V(1-\phi_{Br})\rho_w$ mass of water, where $\rho_w = 1000\,\text{kg/m}^3$ is the density of water. Therefore,

$$\text{molality} = \frac{\phi_{Br}\rho_{Br}/M_{Br}}{(1-\phi_{halide})\rho_w}.$$

The analogous relation applies to chlorine using a molar mass of $M_{Cl} = 0.0355\,\text{kg/mol}$ and a condensed density of $\rho_{Cl} = 1560\,\text{kg/m}^3$. Figure 7.1 shows plots of the functional form measured by Cohen et al. converted to volume fraction. As the plot shows, the two functions agree to within 6% of each other up to the volume fraction of bromide found in pure PVBTMA$\left[\text{Br}^-\right]$. We expect the equations of state for PVBTMA$\left[\text{Br}^-\right]$ and PVBTMA$\left[\text{Cl}^-\right]$ to be in similar agreement. Therefore, it should be acceptable that we use

59
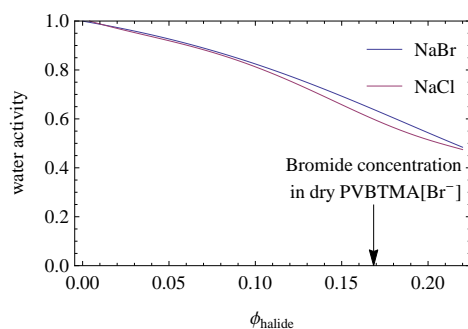
Figure 7.1. Water activity of two salt solutions, NaBr and NaCl (top and bottom, respectively) from data collected by Cohen, et al. [2]. The molality measured by Cohen is converted here to volume fraction of Br or Cl, respectively, as described in Section 7.1. The near agreement of the two curves validates our use of PVBTMA$\left[Br^-\right]$ in the membrane sample (Section 3.3 and PVBTMA$\left[Cl^-\right]$ in the untethered DVS measurements (Section 3.4.3).

the chlorinated form of the hydrophilic block in Section 3.4 to make predictions about the brominated membrane.

7.2 Scheutjens-Fleer illustration

Equations 2.9, 2.10, and 2.11 use the "Scheutjens-Fleer trick" to streamline the calculation on the local concentration $\langle \phi(\zeta) \rangle$. Here, we demonstrate the efficiency gained in a small-scale example. Table 7.1 illustrates a direct calculation over all chain conformations, versus Table 7.2 which uses the Scheutjens-Fleer trick. Both methods are applied to a 3-segment chain, using the segment Boltzmann factors, $T_\zeta \equiv \exp\left[-\mu(\zeta)/k_B T\right]$. Naïvely, to compute the Boltzmann-weighted average chain profile, $\langle \phi(\zeta) \rangle$, one would follow Table 7.1, enumerating all the conformations, calculating the relative probability, R, of each conformation, and computing the profile using equation 2.7. This is computationally expensive as there are on the order of 3^n conformations. The Scheutjens-Fleer trick is much more efficient. It involves an ostensibly similar calculation, shown in Table 7.2, performed once for i increasing and again for i decreasing. The difference in workload is that each term

ζ_1	ζ_2	ζ_3	$\lambda(\zeta_2 - \zeta_1)$	$\lambda(\zeta_3 - \zeta_2)$	$R(\{\zeta\})$
1	1	1	4	4	$16T_1^3$
1	2	1	1	1	$T_1^2 T_2$
1	1	2	4	1	$4T_1^2 T_2$
1	2	2	1	4	$4T_1 T_2^2$
1	2	3	1	1	$T_1 T_2 T_3$

Table 7.1: A direct calculation of the relative probability, R, of all five possible conformations of a 3-segment chain via equation 2.6. The position of each segment i is given by ζ_i. The redundancy factors, λ, are defined in equation 2.5. Here, T_ζ is shorthand for the Boltzmann factor at position ζ. This method does not scale well, requiring $\sim 3^n$ calculations.

is immediately computed to a numerical value, so the algebraic complexity does not grow. Even though information is lost by collapsing the terms, the trick is that the profile $\langle \phi(\zeta) \rangle$ can still by combining both versions of the calculation in a clever way, shown in equation 2.8.

7.3   Half-integer mirror boundary

Section 2.3 describes how to find the self-consistent polymer volume fraction profile for a total hydrophilic width of $2m$. To get more resolution, the method can also accommodate odd-integer spacings by shifting the mirror boundary condition from the end of the mth Kuhn cell to the center. This modifies equations 2.9 and 2.10 for $\zeta = m$ to:

$$G_{1 \to i+1}^{1 \to m} = \exp[-u_K(m)] \left\{ 2G_{1 \to i}^{1 \to m-1} + 4G_{1 \to i}^{1 \to m} \right\},$$

and

$$G_{(i-1) \to n}^{m \to *} = \exp[-u_K(m)] \left\{ 2G_{i \to n}^{m-1 \to *} + 4G_{i \to n}^{m \to *} \right\},$$

respectively. Cell m is then divided between the left and right sides of the lamella.

$G^{1\to\zeta}_{1\to i}$	$\zeta=1$	$\zeta=2$	$\zeta=3$
$i=1$	T_1	0	0
	$4T_1 \downarrow 1T_2 \searrow$		
$i=2$	$4T_1^2$	T_1T_2	0
	$4T_1 \downarrow 1T_2 \searrow$	$\swarrow\ 1T_1\ 4T_2 \downarrow 1T_3 \searrow$	
$i=3$	$16T_1^3+T_1^2T_2$	$4T_1^2T_2+4T_1T_2^2$	$T_1T_2T_3$

$G^{\zeta\to*}_{i\to 3}$	$\zeta=1$	$\zeta=2$	$\zeta=3$
$i=1$	$16T_1^3+5T_1^2T_2+4T_1T_2^2+T_1T_2T_3$	N/A	N/A
	$4T_1 \uparrow$	$\nwarrow\ 1T_2$	
$i=2$	$4T_1^2+T_1T_2$	$T_1T_2+4T_2^2+T_2T_3$	N/A
	$4T_1 \uparrow \nearrow 1T_2$	$\nwarrow\ 1T_1 \uparrow 4T_2$	$\nwarrow\ 1T_2$
$i=3$	T_1	T_2	T_3

Table 7.2: A calculation of the Scheutjens-Fleer Green's functions: $G^{1\to\zeta}_{1\to i}$ (top) via equation 2.9, and $G^{\zeta\to*}_{i\to 3}$ (bottom) via equation 2.10. Row $i=1$ is the first segment, which has Boltzmann factor T_1. The $G^{1\to\zeta}_{1\to i}$ values are computed starting in the top row and building downward by multiplying the elements of the previous row by λT_ζ, as indicated by the arrows. Similarly, the $G^{\zeta\to*}_{i\to 3}$ terms are computed from bottom to top. Although this process is similar to the direct enumeration of states in Table 7.1, it scales as $m \cdot n$ since the sums can be computed immediately.
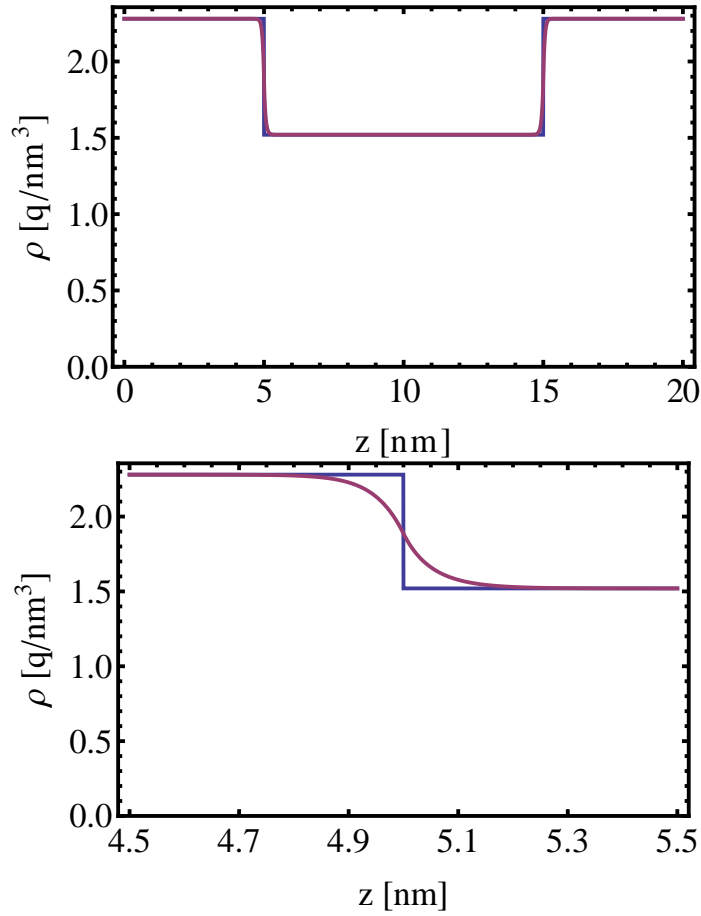
Figure 7.2. The Scheutjens-Fleer calculation ignores electric dipole effects. A Poisson-Boltzmann calculation shows that this is a valid assumption. Even in a worst-case scenario where the polymer profile is discontinuous, the free-charge concentration closely follows it (a). Zooming into the region of the discontinuity (b), it is apparent that the Debye screening length is much smaller than the resolution of the Scheutjens-Fleer calculation, ℓ_K.

7.4   Poisson-Boltzmann

Evidently, electric fields develop in a polyelectrolyte brush, but these turn out to be negligible. In Chapter 4, we inferred the free energy cost of a polymer-water mixture from the water uptake experiment (DVS) of the untethered hydrophilic block, implicitly assuming that the properties are equivalent. This assumption could break down, however, if the free ion distribution changes in response to the tethering forces. Then, an electrostatic gradient

could develop that was not accounted for in the analysis. Here, we show that the effect is miniscule.

The free ions are not tied down to their counter-ions on the polyelectrolyte and are free thermally diffuse. Since the polyelectrolyte and the free ions are subject to different constraints, they follow different spatial distributions and this difference produces electric fields. To place a bound on this effect, we analyze the worst-case scenario, where the polyelectrolyte distribution jumps discontinuously from one value to another (Figure 7.2). The free ion distribution is then determined by the Boltzmann weighting:

$$\rho_-(z) = \rho_I \exp\left[\frac{-q\Psi(z)}{k_B T}\right],$$

where $\Psi(z)$ is the electric potential at point z, q is the elementary charge, and ρ_I is the charge density at the interface due to OH^- (this sets the gauge by requiring $\Psi = 0$ at the interface). Plugging this expression into the Poisson equation gives the Poisson-Boltzmann equation:

$$\frac{\partial}{\partial z}\left[\varepsilon(z)\frac{\partial}{\partial z}\Psi(z)\right] = -4\pi\rho_+(z) - 4\pi\rho_I \exp\left[\frac{-q\Psi(z)}{k_B T}\right].$$

Here, $\varepsilon(z)$ is the background electric permittivity. To avoid the problem of a discontinuous function for $\varepsilon(z)$, here we use a uniform permittivity, $\varepsilon(z) = 40\varepsilon_0$, an estimate that is roughly midway between that for hydrocarbons and water. To find $\rho_+(z)$, we first estimate that the charge density for pure $PVBTMA\left[Cl^-\right]$ is roughly $3.8q\,nm^{-3}$. This value is combined with a contrived "worst-case" step function to give the fixed charge density distribution. Because the Poisson-Boltzmann equation is highly non-linear and very unstable

64

numerically, we isolate a 1 nm region containing the step function:

$$\rho_+(z) = 3.8q\,\mathrm{nm}^{-3} \begin{cases} 4/10 & z > 0.5\,\mathrm{nm} \\ 6/10 & z < 0.5\,\mathrm{nm} \end{cases}$$

The differential equation is order 2 and so requires two boundary conditions. We set $\Psi(0)$ such that $\rho_-(0) = \rho_+(0)$, and iterate choices of $\Psi'(0)$ until $\rho_-(1) = \rho_+(1)$ where $z = 0$ and $z = 1$ are the left and right boundary points of the 1 nm calculation box. Note that if $\Psi'(0)$ and $\Psi'(1)$ both vanished, then the solution outside the box will satisfy $\rho_-(z) = \rho_+(z)$. Such would be the case if the calculation domain were large enough to contain the transient due to the sharp step function. This turns out to be the case. $\Psi'(0)$ turns out to be $-5.76\ldots \times 10^{-6}\,\mathrm{V/nm}$ and $\Psi'(1) = -3.13\ldots \times 10^{-5}\,\mathrm{V/nm}$, which are both quite small for the scales involved in the problem. The characteristic width of the mismatch between the fixed and the free ion distributions is given by the Debye length,

$$\lambda_D = \left(\frac{\varepsilon k_B T}{\rho q} \right)^{1/2} \approx 0.17\,\mathrm{nm}.$$

REFERENCES

[1] T.-H. Tsai, *Ionic Copolymers for Alkaline Anion Exchange Membrane Fuel Cells (AAEMFCs)*. PhD thesis, University of Massachusetts Amherst, 2014.

[2] M. D. Cohen, R. C. Flagan, and J. H. Seinfeld, "Studies of concentrated electrolyte solutions using the electrodynamic balance. 1. water activities for single-electrolyte solutions," *J. Phys. Chem.-US*, vol. 91, no. 17, pp. 4563–4574, 1987.

[3] J. R. Varcoe, P. Atanassov, D. R. Dekel, A. M. Herring, M. A. Hickner, P. A. Kohl, A. R. Kucernak, W. E. Mustain, K. Nijmeijer, K. Scott, T. Xu, and L. Zhuang, "Anion-exchange membranes in electrochemical energy systems," *Energy Environ. Sci.*, vol. 7, no. 10, pp. 3135–3191, 2014.

[4] W. R. Grove, "On voltaic series and the combination of gases by platinum," *Lond. Edinb. Dubl. Phil. Mag.*, vol. 14, no. 86, pp. 127–130, 1839.

[5] G. F. McLean, T. Niet, S. Prince-Richard, and N. Djilali, "An assessment of alkaline fuel cell technology," *Int. J. Hydrogen Energ.*, vol. 27, no. 5, pp. 507–526, 2002.

[6] J. R. Varcoe and R. C. Slade, "Prospects for alkaline anion-exchange membranes in low temperature fuel cells," *Fuel Cells*, vol. 5, no. 2, pp. 187–200, 2005.

[7] E. Gülzow and M. Schulze, "Long-term operation of AFC electrodes with CO_2 containing gases," *J. Power Sources*, vol. 127, no. 1, pp. 243–251, 2004.

[8] M. Schulze and E. Gülzow, "Degradation of nickel anodes in alkaline fuel cells," *J. Power Sources*, vol. 127, no. 1, pp. 252–263, 2004.

[9] J. Larminie and A. Dicks, *Fuel Cell Systems Explained*. J. Wiley, 2003.

[10] W. Grot, *Fluorinated Ionomers*. Elsevier Science, 2nd ed., 2011.

[11] Z. Qi and A. Kaufman, "Low Pt loading high performance cathodes for PEM fuel cells," *J. Power Sources*, vol. 113, no. 1, pp. 37–43, 2003.

[12] S. Gamburzev, K. Petrov, and A. J. Appleby, "Silver–carbon electrocatalyst for air cathodes in alkaline fuel cells," *J. Appl. Electrochem.*, vol. 32, no. 7, pp. 805–809, 2002.

[13] N. Wagner, M. Schulze, and E. Gülzow, "Long term investigations of silver cathodes for alkaline fuel cells," *J. Power Sources*, vol. 127, no. 1, pp. 264–272, 2004.

[14] B. Xing and O. Savadogo, "Hydrogen/oxygen polymer electrolyte membrane fuel cells (PEMFCs) based on alkaline-doped polybenzimidazole (PBI)," *Electrochem. Commun.*, vol. 2, no. 10, pp. 697–702, 2000.

[15] A. C. Cope and E. R. Trumbull, "Olefins from amines: the hofmann elimination reaction and amine oxide pyrolysis," *Org. Reactions*, 1960.

[16] E. Trostyanskaya and S. Makarova, "Anion exchangers onium class of compounds," *J. Appl. Chem.-USSR*, vol. 39, no. 8, p. 1754, 1966.

[17] Q. H. Zeng, Q. L. Liu, I. Broadwell, A. M. Zhu, Y. Xiong, and X. P. Tu, "Anion exchange membranes based on quaternized polystyrene-block-poly (ethylene-ran-butylene)-block-polystyrene for direct methanol alkaline fuel cells," *J. Membrane Sci.*, vol. 349, no. 1, pp. 237–243, 2010.

[18] D. J. Pickett, *Electrochemical Reactor Design*. Elsevier Publishing Company, 1979.

[19] N. Asano, M. Aoki, S. Suzuki, K. Miyatake, H. Uchida, and M. Watanabe, "Aliphatic/aromatic polyimide ionomers as a proton conductive membrane for fuel cell applications," *J. Am. Chem. Soc.*, vol. 128, no. 5, pp. 1762–1769, 2006.

[20] U. Pasaogullari and C. Wang, "Liquid water transport in gas diffusion layer of polymer electrolyte fuel cells," *J. Electrochem. Soc.*, vol. 151, no. 3, pp. A399–A406, 2004.

[21] X. Huang, R. Solasi, Y. Zou, M. Feshler, K. Reifsnider, D. Condit, S. Burlatsky, and T. Madden, "Mechanical endurance of polymer electrolyte membrane and PEM fuel cell durability," *J. Polym. Sci. Pol. Phys.*, vol. 44, no. 16, pp. 2346–2357, 2006.

[22] L. Lebrun, N. Follain, and M. Metayer, "Elaboration of a new anion-exchange membrane with semi-interpenetrating polymer networks and characterisation," *Electrochim. Acta*, vol. 50, no. 4, pp. 985–993, 2004.

[23] M. Singh, O. Odusanya, G. M. Wilmes, H. B. Eitouni, E. D. Gomez, A. J. Patel, V. L. Chen, M. J. Park, P. Fragouli, H. Iatrou, N. Hadjichristidis, D. Cookson, and N. P. Balsara, "Effect of molecular weight on the mechanical and electrical properties of block copolymer electrolytes," *Macromolecules*, vol. 40, no. 13, pp. 4578–4585, 2007.

[24] F. S. Bates and G. H. Fredrickson, "Block copolymer thermodynamics: theory and experiment," *Annu. Rev. Phys. Chem.*, vol. 41, no. 1, pp. 525–557, 1990.

[25] K. R. Shull, K. I. Winey, E. L. Thomas, and E. J. Kramer, "Segregation of block copolymer micelles to surfaces and interfaces," *Macromolecules*, vol. 24, no. 10, pp. 2748–2751, 1991.

[26] G. Gebel, "Structural evolution of water swollen perfluorosulfonated ionomers from dry membrane to solution," *Polymer*, vol. 41, no. 15, pp. 5829–5838, 2000.

[27] M. W. Matsen and M. Schick, "Stable and unstable phases of a diblock copolymer melt," *Phys. Rev. Lett.*, vol. 72, no. 16, p. 2660, 1994.

[28] M. J. Park and N. P. Balsara, "Phase behavior of symmetric sulfonated block copolymers," *Macromolecules*, vol. 41, no. 10, pp. 3678–3687, 2008.

[29] P. Knychała, M. Banaszak, M. J. Park, and N. P. Balsara, "Microphase separation in sulfonated block copolymers studied by Monte Carlo simulations," *Macromolecules*, vol. 42, no. 22, pp. 8925–8932, 2009.

[30] E. Helfand and Z. R. Wasserman, "Block copolymer theory. 4. narrow interphase approximation," *Macromolecules*, vol. 9, no. 6, pp. 879–888, 1976.

[31] K. M. Hong and J. Noolandi, "Theory of inhomogeneous multicomponent polymer systems," *Macromolecules*, vol. 14, no. 3, pp. 727–736, 1981.

[32] M. J. Park and N. P. Balsara, "Anisotropic proton conduction in aligned block copolymer electrolyte membranes at equilibrium with humid air," *Macromolecules*, vol. 43, no. 1, pp. 292–298, 2009.

[33] D. Herbst and W. T, "Predicting inhomogeneous water absorption in an ionic diblock polymer membrane," in *Bulletin of the American Physical Society*, vol. 58, March 2013. A31.7.

[34] A. M. Herring, M. A. Vandiver, A. M. Maes, H. N. Sarode, E. B. Coughlin, D. M. Knauss, Y. Yan, G. E. Lindberg, C. Knight, G. A. Voth, *et al.*, "Fundamental studies of alkaline exchange membranes towards optimization in a fuel cell environment," *ECS Transactions*, vol. 50, no. 2, pp. 2059–2066, 2013.

[35] X. C. Chen, D. T. Wong, S. Yakovlev, K. M. Beers, K. H. Downing, and N. P. Balsara, "Effect of morphology of nanoscale hydrated channels on proton conductivity in block copolymer electrolyte membranes," *Nano Lett.*, vol. 14, no. 7, pp. 4058–4064, 2014.

[36] G. H. Fredrickson, V. Ganesan, and F. Drolet, "Field-theoretic computer simulation methods for polymers and complex fluids," *Macromolecules*, vol. 35, no. 1, pp. 16–39, 2002.

[37] Y.-L. S. Tse, H. N. Sarode, G. E. Lindberg, T. A. Witten, Y. Yang, A. M. Herring, and G. A. Voth, "Chloride enhances fluoride mobility in anion exchange membrane/polycationic systems," *J. Phys. Chem. C*, vol. 118, no. 2, pp. 845–853, 2014.

[38] G. S. Grest and M. Murat, "Structure of grafted polymeric brushes in solvents of varying quality: a molecular dynamics study," *Macromolecules*, vol. 26, no. 12, pp. 3108–3117, 1993.

[39] S. F. Edwards, "The statistical mechanics of polymers with excluded volume," *Proc. Phys. Soc.*, vol. 85, no. 4, p. 613, 1965.

[40] P.-G. de Gennes, "Polymers at an interface. 2. interaction between two plates carrying adsorbed polymer layers," *Macromolecules*, vol. 15, no. 2, pp. 492–500, 1982.

[41] S. Milner, T. Witten, and M. Cates, "Theory of the grafted polymer brush," *Macromolecules*, vol. 21, no. 8, pp. 2610–2619, 1988.

[42] J. Scheutjens and G. Fleer, "Statistical theory of the adsorption of interacting chain molecules. 1. partition function, segment density distribution, and adsorption isotherms," *J. Phys. Chem.-US*, vol. 83, no. 12, pp. 1619–1635, 1979.

[43] G. J. Fleer, M. A. C. Stuart, J. M. H. M. Scheutjens, T. Cosgrove, and B. Vincent, *Polymers at Interfaces*. Springer, 1993.

[44] M. Whitmore and J. Noolandi, "Theory of adsorbed block copolymers," *Macromolecules*, vol. 23, no. 13, pp. 3321–3339, 1990.

[45] K. R. Shull, "Theory of end-adsorbed polymer brushes in polymeric matrices," *J. Chem. Phys.*, vol. 94, no. 8, pp. 5723–5738, 1991.

[46] F. W. Cain, R. H. Ottewill, and J. B. Smitham, "Direct measurements of the interaction between adsorbed macromolecular layers," *Faraday Discuss. Chem. Soc.*, vol. 65, pp. 33–42, 1978.

[47] J. Klein, "Forces between mica surfaces bearing layers of adsorbed polystyrene in cyclohexane," *Nature*, vol. 288, no. 5788, pp. 248–250, 1980.

[48] N. Dan and M. Tirrell, "Self-assembly of block copolymers with a strongly charged and a hydrophobic block in a selective, polar solvent. micelles and adsorbed layers," *Macromolecules*, vol. 26, no. 16, pp. 4310–4315, 1993.

[49] J. M. H. M. Scheutjens and G. J. Fleer, "Interaction between two adsorbed polymer layers," *Macromolecules*, vol. 18, no. 10, pp. 1882–1900, 1985.

[50] P.-Y. Lai and K. Binder, "Structure and dynamics of polymer brushes near the Θ point: a Monte Carlo simulation," *J. Chem. Phys.*, vol. 97, no. 1, pp. 586–595, 1992.

[51] A. Karim, S. Satija, J. Douglas, J. Ankner, and L. Fetters, "Neutron reflectivity study of the density profile of a model end-grafted polymer brush: influence of solvent quality," *Phys. Rev. Lett.*, vol. 73, no. 25, p. 3407, 1994.

[52] C. Lai, W. B. Russel, and R. A. Register, "Phase behavior of styrene-isoprene diblock copolymers in strongly selective solvents," *Macromolecules*, vol. 35, no. 3, pp. 841–849, 2002.

[53] G. Fredrickson, *The Equilibrium Theory of Inhomogeneous Polymers*. Internat. Ser. Monogr. Phys., OUP, Oxford, 2006.

[54] H. Yamakawa, *Modern Theory of Polymer Solutions. Electronic Edition*. Harper & Row, 1971.

[55] W. Press, *Numerical Recipes 3rd Edition: The Art of Scientific Computing*. Cambridge University Press, 2007.

[56] L. Reichl, *A Modern Course in Statistical Physics*. Wiley, 1998.

[57] R. S. Bhavsar, S. C. Kumbharkar, and U. K. Kharul, "Polymeric ionic liquids (PILs): Effect of anion variation on their CO_2 sorption," *J. Membrane Sci.*, vol. 389, pp. 305–315, 2012.

[58] J. Gotro and W. W. Graessley, "Model hydrocarbon polymers: rheological properties of linear polyisoprenes and hydrogenated polyisoprenes," *Macromolecules*, vol. 17, no. 12, pp. 2767–2775, 1984.

[59] J. Brandrup, E. H. Immergut, and E. A. Grulke, *Polymer Handbook, 4th Ed.* Wiley, 1999.

[60] Y. Takahashi, N. Matsumoto, S. Iio, H. Kondo, I. Noda, M. Imai, and Y. Matsushita, "Concentration dependence of radius of gyration of sodium poly (styrenesulfonate) over a wide range of concentration studied by small-angle neutron scattering," *Langmuir*, vol. 15, no. 12, pp. 4120–4122, 1999.

[61] T. Odijk, "Polyelectrolytes near the rod limit," *J. Poly. Sci.: Poly. Phys. Ed.*, vol. 15, no. 3, pp. 477–483, 1977.

[62] M. D. Gehlsen, P. A. Weimann, F. S. Bates, S. Harville, J. W. Mays, and G. D. Wignall, "Synthesis and characterization of poly (vinylcyclohexane) derivatives," *J. Polym. Sci. Pol. Phys.*, vol. 33, no. 10, pp. 1527–1536, 1995.

[63] K. R. Shull and K. I. Winey, "Homopolymer distributions in lamellar copolymer/homopolymer blends," *Macromolecules*, vol. 25, no. 10, pp. 2637–2644, 1992.

[64] M. Rubinstein and R. H. Colby, *Polymer Physics*. OUP Oxford, 2003.

[65] P. J. Flory, "Thermodynamics of high polymer solutions," *J. Chem. Phys.*, vol. 9, no. 8, p. 660, 1941.

[66] M. L. Huggins, "Solutions of long chain compounds," *J. Chem. Phys.*, vol. 9, p. 440, 1941.

[67] D. Lide, *CRC Handbook of Chemistry and Physics, 85th Edition*. Taylor & Francis, 2004.

[68] G. S. Manning, "Limiting laws and counterion condensation in polyelectrolyte solutions i. colligative properties," *J. Chem. Phys.*, vol. 51, no. 3, pp. 924–933, 1969.

[69] L. Wang and V. A. Bloomfield, "Osmotic pressure of polyelectrolytes without added salt," *Macromolecules*, vol. 23, no. 3, pp. 804–809, 1990.

[70] K. P. Burnham and D. R. Anderson, *Model Selection and Multimodel Inference: a Practical Information-Theoretic Approach*. Springer, 2nd ed., 1998.

[71] J. Bockris and A. Reddy, *Volume 1: Modern Electrochemistry: Ionics*. Springer, 1998.